Master thesis

Long-External Cavity DBR Diode Laser implemented with an Optical Fiber

Felix Ernst Bösch, BSc

Submitted to the
Faculty of Mathematics, Computer Science and Physics of the
University of Innsbruck

in partial fulfilment of the requirements for the degree of
master of science (MSc.)

Supervised by
Univ.-Prof. Dr. Rudolf Grimm

9. November 2021

Eidesstattliche Erklärung

Ich erkläre hiermit an Eides statt durch meine eigenständige Unterschrift, dass ich die vorliegende Arbeit selbstständig verfasst und keine anderen als die angegebenen Quellen und Hilsmittel verwendet habe. Alle Stellen, die wörtlich oder inhaltlich den angegebenen Quellen entnommen wurden, sind als solche kenntlich gemacht.

Die vorliegende Arbeit wurde bisher in gleicher oder ähnlicher Form noch nicht als Magister-/Master-/Diplomarbeit/Dissertation eingereicht.

Datum	Unterschrift

Abstract

This master thesis contains a description and realisation of an external cavity DBR diode laser (ECDL) system with the use of a retro-reflecting optical fiber to provide optical feedback. A first iteration of the laser system uses standard mirror mounts in the ECDL path. The next improved version eliminates all moveable components in the ECDL system and makes use of two Risley prism pairs to steer the beam. In addition, a custom-made aluminium housing was built to accommodate all optical elements of the ECDL. The novel approach of using a retro-reflecting optical fiber, where the light is coupled with two Risley prism pairs will be tested. To further stabilise the laser system, modulation transfer spectroscopy (MTS) on a Cesium vapour cell is performed. With the help of a proportional-, integral- and derivative- (PID) servo, the MTS error signal is used to control the system electronically and match the laser's frequency to the Cesium D2-line, which acts as an absolute frequency reference. The first version of the ECDL system achieves a laser linewidth of 72(3) kHz. This is improved with the second ECDL setup, where moveable parts are removed, down to 5,7(2) kHz. The bare DBR diode has a linewidth on the order of 10 MHz, which yields a reduction in linewidth of four orders of magnitude.

Kurzfassung

In dieser Masterarbeit wird ein DBR Dioden Laser mit einem langen, externen Resonator realisiert. Der externe Laserresonator wird dabei mit einer selbst-reflektierenden optischen Glasfaser aufgebaut. Die erste Version des Laser-Systems wird mit klassischen Spiegel-Halterungen aufgebaut. Eine zweite, verbesserte Version des Laser-Systems wird ohne diese beweglichen Spiegel-Halter aufgebaut und verwendet stattdessen zwei Risley-Prismenpaare, um den Laserstrahl zu lenken. Zudem wird eine maßgeschneiderte Box aus Aluminium extra für das Lasersystem angefertigt, um externe Einflüsse wie Luftstöße und Staub zu minimieren. Dieser neue Ansatz, einen Diodenlaser mit externem Resonator mithilfe einer selbstreflektierenden optischen Faser, in die das Laser Licht mit zwei Prismen Paaren eingekoppelt wird, soll hier getestet werden. Die Spektroskopie-Technik *Modulation Transfer Spectroscopy* wird an Cäsium Atomen bei Raumtemperatur angewendet. Das daraus gewonnene Fehlersignal wird mithilfe eines Proportional-, Integral-, und Differential-Verstärkers verwendet, um das Lasersystem elektronisch zu kontrollieren. Der Cäsium D2-Übergang agiert dabei als absolute Frequenzreferenz. Die erste Version des Lasers erreicht eine Linienbreite von 72(3) kHz. Dieser Wert wird mit der zweiten Version, bei der alle beweglichen Teile entfernt wurden, verbessert auf 5,7(2) kHz. Die DBR Laser Diode ohne optische Rückkopplung hat eine Linienbreite in der Größenordnung von 10 MHz. Somit wird eine Verkleinerung der Linienbreite um vier Größenordnungen erzielt.

Table of contents

1 Introduction

The field of laser physics has evolved rapidly over the past decade and has revolutionised experimental physics and in particular for our interest quantum physics. About 60 years ago, semiconductor diode lasers were first demonstrated by the works of Bernard and Duraffourg [18], Basov *et. al.* [19], Nathan [21], Holonyak and Bevacqua [20] and Hall *et. al.* [22] at the beginning of the 1960s. About 10 years later at the beginning of the 1970s, semiconductor lasers were already found in the fields of optical data storage, fiber optics and free space communication. But the simple p-n junction devices back then were far away from the laser diodes we know today. Large injection currents and the need of cryogenic temperatures (from 120 K down to absolute zero temperature) challenged the practical use of such early devices. However, the works of Hayashi *et. al.* [27] and Alferov *et. al.* [28] in 1970 and of course the development in the design of double heterostructure laser devices led to a breakthrough. It was then possible to build reliable diode lasers working with far lower injection currents and at room temperature [58]. It can be said that the development of semiconductor lasers is at eye level with the transistor and the integrated circuit, regarding their influence on modern day technology. The further development of diode lasers led to more complicated devices that could provide single-mode operation. For high power output, diode laser arrays were built and also the distributed feedback lasers have been developed [54]. These have been made possible by the use of two new key growth technologies, namely molecular beam epitaxy (MPE) and metal organic chemical vapour deposition (MOCVD). With this, uniform material deposition and quantum well active layers were developed. In addition, many kinds of bulk gas and solid state lasers were replaced by semiconductor lasers, since the development of new diode laser materials made it possible to cover more wavelengths than ever before with a semiconductor device. In contrast to bulk gas and solid state lasers, diode lasers have the advantage of being low-cost, more compact and having great efficiency.

In this Master thesis, a distributed Bragg reflector (DBR) laser diode is used to build a tunable long-external-cavity diode laser (ECDL), where the external cavity is formed inside a retro-reflecting optical fiber. In general, a tunable ECDL system utilises a semiconductor diode laser, a collimator to couple the laser diode's output and some external mode-selection filter. However, there are many different configurations to build an ECDL. In 1964, shortly after the first successful operation of a diode laser was demonstrated, a diode laser was first coupled to an external cavity by Crowe and Craig [23]. The most common example of a ECDL is the Littrow and the Littman-Metcalf configuration, where a grating provides the optical feedback. The grating also serves as the mode-selective element and tunes the wavelength. These ECDL configurations will be discussed in more detail in section 2.6.

2 Basic Considerations

2.1 Laser Overview

A laser is a device that emits light. The name comes from '**L**ight **A**mplified by **S**timulated **E**mission of **R**adiation', which basically describes the fundamental principle of how a laser works.

2.2 Basics of Atom-Light Interaction

To understand how a semiconductor laser works, we need to start at the fundamentals of light absorption and emission in an atom. Every electron in an atom or a molecule has it's own stationary states, in which the atom has specific energy levels, see figure 1. When an electron in the atom makes a transition between different states, the atom radiates in terms of light emission. This light emission is always related to the energy difference between the two states where a transition

happens

$$\nu = \frac{E_\mathrm{f} - E_\mathrm{i}}{h}, \tag{1}$$

where ν is the frequency of the emitted light, E_i (E_f) is the energy of the initial (final) state of the transition and $h = 6.62607015 \cdot 10^{-34}\ \frac{\mathrm{J}}{\mathrm{Hz}}$ is Planck's constant [8].

When light interacts with an atom (or molecule), there are three possible scenarios, shown in figure 2. When the atom is in the initial state E_i and light is incident on the atom with frequency $\nu = \nu_0$, where ν_0 is the transition frequency from E_i to E_f, the atom will absorb the energy of the light with a very high probability and make a transition to an excited state E_f. This process is called resonant absorption (figure 2 (a)).

The second process is called spontaneous emission (figure 2 (b)). When an electron is excited to a state E_f, it has the tendency to relax back to the initial state with energy E_i. This will most probably happen after a specific lifetime τ of the excited state. When the electron relaxes back to the initial state, energy in form of light is emitted, where again the emitted photon has a frequency given by the energy difference of the two states $\nu = (E_\mathrm{f} - E_\mathrm{i})/h$. The important thing to note here is though, that the photons are emitted in random directions and with random phases. Therefore, the emitted light is incoherent.

The third process is the so-called stimulated emission. Without this process, there would be no lasers, since this is what generates the coherent laser radiation. In figure 2 (c), an excited atom with it's electron in the excited level E_f is shown. Instead of leaving the atom there and waiting till it relaxes spontaneously, resonant light is incident on the atom with $\nu = \nu_0$. This stimulation of light forces the atom to undergo a transition from E_f to E_i. During this transition, the emitted photon is generated as a new addition to the incident light. The emitted photon has the same direction and phase as the incident light, and therefore coherent light is generated during this process.

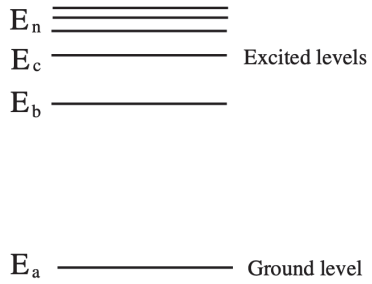

Figure 1: Energy level diagram for no specific atom. Graphic taken from [61].

2.3 Conditions for Lasing in a Semiconductor Laser Diode

When a semiconductor laser diode is manufactured, specific atoms (or molecules) are squeezed together to form a solid crystal. This has the effect, that the discrete energy levels of atoms (or molecules) smear together to form energy bands, see figure 3. For the atoms to generate laser light, two conditions need to be fulfilled: Firstly, there need to be more atoms in an excited energy band than there are atoms in the ground energy band. This is also called population inversion. Secondly, one needs to have more stimulated emissions than spontaneous ones. To achieve this, a resonator is used to feed back already generated light into the active medium of a laser diode to further enhance the generation of stimulated emissions.

Let us first take a closer look at population inversion. In figure 4 (a) a typical energy band scheme of a semiconductor is shown. The lower energy band is the valence band and the upper energy band the conduction band. If we assume a temperature of $T = 0$ K, all the electrons will remain in the

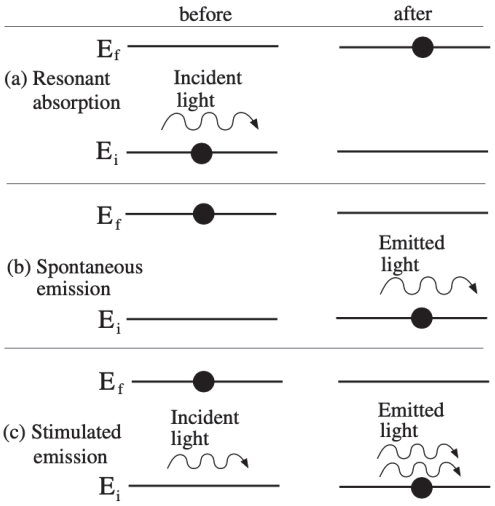

Figure 2: Interaction of light with an atom. The three fundamental processes: (a) Resonant absorption, (b) Spontaneous emission and (c) stimulated emission. Graphic taken from [61].

valence band. At finite temperature, some electrons may be excited to the conduction band, but most of the population will remain in the lower energy band. The most common way to create a population inversion is to drive the semiconductor crystal with a current. The energy gap between the upper boundary of the valence band and the lower boundary of the conduction band is called gap energy E_g and since there are no states for the electrons to be occupied, this region is forbidden. When electrons get excited into the conduction band, they take some energy E_2, from which they spontaneously relax to the lowest possible energy state in the conduction band after very short time ($\approx$ ps). The occupation probability (of electrons) in the conduction band is

$$f_\mathrm{c} = \frac{1}{1 + e^{(E_2 - E_\mathrm{Fc})/(k_\mathrm{B} t)}}, \tag{2}$$

where E_2 is some given energy value in the conduction band, E_Fc is the upper boundary of energy levels in the conduction band (quasi-Fermi level) and $k_\mathrm{B} = 1.380649 \cdot 10^{-23}\ \frac{\mathrm{J}}{\mathrm{K}}$ [7] is the Boltzmann constant. Now when some electrons from the valence band are excited to the conduction band, the leftover electrons in the valence band relax to the lowest possible states that are now free to be occupied. This creates a new upper boundary energy level in the valence band, the quasi-Fermi level E_Fv. The occupation probability (of holes) in the valence band is

$$f_\mathrm{v} = \frac{1}{1 + e^{(E_1 - E_\mathrm{Fv})/(k_\mathrm{B} t)}}, \tag{3}$$

where E_1 is some energy level in the valence band. To clarify why these new boundary energy levels are called quasi-Fermi energy levels, remember: At $T = 0$ K, $f(E) = 1$ for $E < E_\mathrm{F}$ and $f(E) = 0$ for $E > E_\mathrm{F}$. Speaking in words, all energy levels below E_F are completely filled, while all energy levels above E_F are empty.

When the population inversion is reached, electrons relax back to the valence band and take the empty holes (=quasi-anti-electron) and during this transition, photons are emitted. The rate of resonant absorption from valence band to conduction band is given by

$$R_{12} = R_r[f_\mathrm{v}(1 - f_\mathrm{c})]. \tag{4}$$

Here, R_r is the transition rate of two levels in the respective band. This equation shows the absorption of a photon to create an electron in the conduction band, where a hole in the valence band is

left over. Next is the rate of stimulated emission from the conduction band to the valence band, given by

$$R_{21} = R_r[f_c(1 - f_v)]. \tag{5}$$

In contrast to R_{12}, this equation shows the stimulated relaxation of an electron in the conduction band, taking a place of a hole in the valence band and therefore generating a new photon into the incident lightfield. The net rate for stimulated emission is therefore

$$R_{net} = R_{21} - R_{12} = R_r(f_c - f_v). \tag{6}$$

To amplify the incident radiation, $f_c > f_v$ is needed (population inversion condition). The next thing we know is that

$$\Delta E_F = E_{Fc} - E_{Fv} > E_2 - E_1 = E_{21} = h\nu, \tag{7}$$

where ν is the emitted photon's frequency. We see that only photons with a frequency $\nu < \Delta E_F$ can be amplified and contribute to the laser radiation. We can introduce another limit for the photon energy, the energy gap E_g

$$\Delta E_F > E_{21} = E_g + \frac{\hbar^2 k^2}{2m_e^*} + \frac{\hbar^2 k^2}{2m_h^*} > E_g, \tag{8}$$

where m_e^* (m_h^*) is the effective mass of an electron (hole). The quasi-Fermi energy levels are dependent on the carrier density n. As already mentioned, some pumping scheme needs to be performed in order to create population inversion in a semiconductor. This can be realised by shining another laser beam into the active semiconductor medium, but the most common thing to do is to apply an electrical current to run through the semiconductor. Now when applying an electrical current, the carrier density n increases. This forces E_{Fc} to increase and E_{Fv} to decrease. With no applied current, we call the carrier density fulfilling the condition

$$E_{Fc}(n) - E_{Fv}(n) = E_g \tag{9}$$

the transparency carrier density n_{tr}. The semiconductor experiences a net gain, if an applied current increases the carrier density until $n > n_{tr}$. When we now place the semiconductor into a suitable resonator and the net gain overcomes losses, the medium starts to generate coherent laser light.

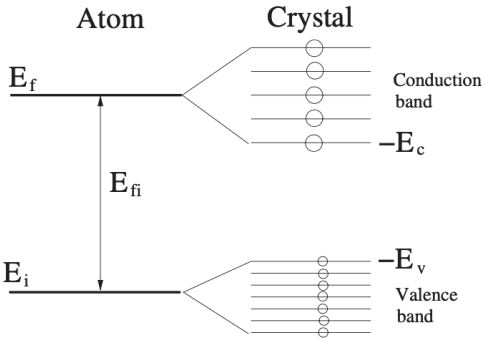

Figure 3: Squeezing atoms (or molecules) into a crystal lets the discrete energy level smear together to form energy bands in the solid. Graphic taken from [61].

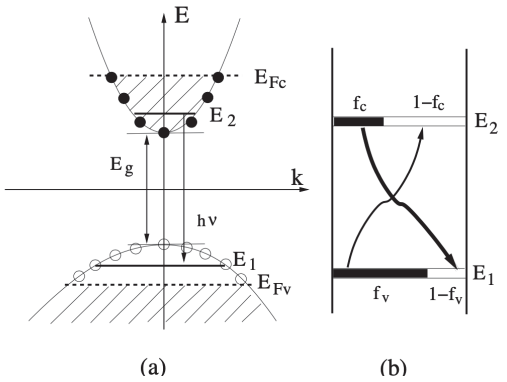

Figure 4: (a) The plot shows electron energy E against the wavenumber k for a semiconductor. For further explanation see text. (b) Occupation probabilities f_v and f_c for the valence band and the conduction band in thermal equilibrium. Graphic taken from [61].

2.4 Important Characteristics of Laser Diodes

In figure 5, a laser diode with a general Fabry-Perot resonator is shown. One can see the structure of the diode as well as the emitted beam. The divergence of the output laser beam is due to the small size of the semiconductor chip, where the beam is diffraction-limited orthogonal and parallel to the junction. This results in the typical elliptical shaped cone of light emitting from a laser diode. The beam divergence in the parallel (orthogonal) plane to the junction is given by $\theta_{\parallel} = 2\lambda/\pi q_{\parallel}$ ($\theta_{\perp} = 2\lambda/\pi q_{\perp}$) respectively, where λ is the lasing wavelength and $q_{\parallel}$ ($q_{\perp}$) are the beam dimensions at full width between $1/e$ points of the electric field for the parallel and orthogonal axis to the junction.

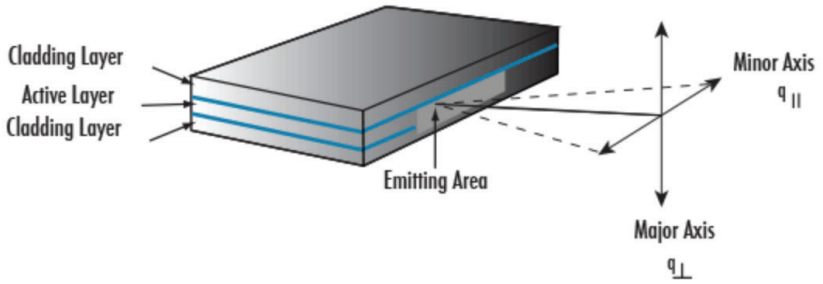

Figure 5: Structure of a general Fabry-Perot laser diode. The divergence of the output beam is also shown. Graphic taken from [5].

2.4.1 Output Power

One of the most important parameters for a diode laser (as well as for any other laser) is the output power. Since diode lasers consist of semiconductor materials, some threshold current needs to be reached in order to achieve lasing. If we look at figure 6, we can see the diode acting like a light emitting diode (LED) below the threshold current. Above the threshold current, population inversion is achieved and coherent laser light is emitted. To determine the threshold current I_th, the linear part of the graph is extrapolated to zero output power, this is shown in figure 6 with ΔP and ΔI.

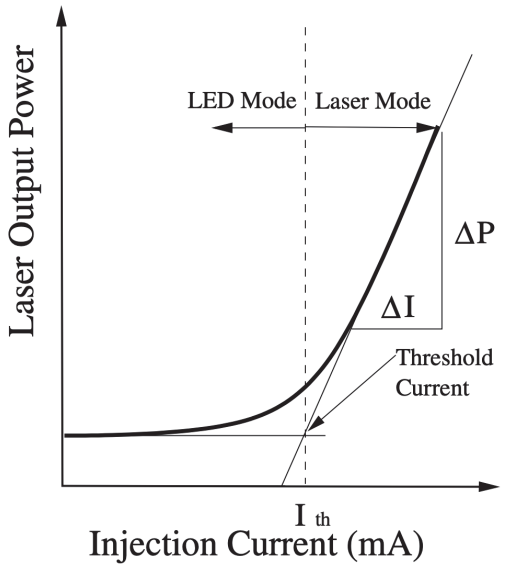

Figure 6: Output power versus injection current for a diode laser. Zero output power is marked with the thin horizontal line. Graphic taken from [61].

2.4.2 Resonance Condition in a Fabry-Perot (FP) Resonator Laser Diode

As already discussed, lasing is not guaranteed by population inversion. One needs to add a resonant cavity to the active medium of a laser diode in order to amplify light, get more stimulated emissions than absorptions and to build up resonances inside the cavity. To understand how stimulated emission takes place and how certain resonances in a laser diode arise, see figure 7. Consider a plane wave E_i incident to the left of the resonator. After entering through the left-hand mirror, the wave becomes $E_\mathrm{i}t_1$, with t_1 being the ratio of transmitted light to incident light on the left mirror. This wave travels through the cavity until it hits the right-hand mirror, where we describe the plane wave as $t_1E_\mathrm{i}e^{-jkd}$ ($k = \beta + j(g - \alpha)$ with β the propagation coefficient, g the gain per unit length and α the internal attenuation per unit length; d the length of the cavity). This wave being incident on the right-hand side mirror, some portion $t_1t_2E_\mathrm{i}e^{-jkd}$ is transmitted and some portion $r_2t_1E_\mathrm{i}e^{-jkd}$ (r_2 is the ratio of reflected light to incident light on the right-hand mirror) is reflected back into the cavity. Note that when the light is reflected by one of the mirrors, a phase shift $e^{i\theta_{1,2}}$ is added theoretically, but for a low-loss medium this can be neglected. The next wave exiting the right-hand side mirror will then be $r_1r_2t_1t_2E_\mathrm{i}e^{-j3kd}$ and so on. We can write down the output wave as

$$E_\mathrm{o} = t_1t_2E_\mathrm{i}e^{-jkd}\left(1 + r_1r_2e^{-2jkd} + (r_1r_2)^2e^{-4jkd} + ...\right). \tag{10}$$

The sum in equation (10) is a geometric progression and we can therefore rewrite the equation to

$$E_\mathrm{o} = E_\mathrm{i}\frac{t_1t_2e^{-jkd}}{1 - r_1r_2e^{-2jkd}}. \tag{11}$$

The condition for oscillation is reached when the denominator in equation (11) goes to zero. Then, a finite output wave E_o is obtained with a zero input wave E_i. In other words, the oscillation condition is reached when

$$r_1r_2e^{-2jkd} = 1, \tag{12}$$

or when inserting $k = \beta + j(g - \alpha)$ defined above

$$r_1r_2e^{-2jd\beta}e^{2(g-\alpha)d} = 1. \tag{13}$$

This oscillation condition describes a wave making a round trip $2d$ in the cavity of length d from the starting plane (mirror with indices 1) to the end plane (mirror with indices 2) and back to the starting plane with same amplitude and phase. When we take into account the confinement factor Γ of the cavity, we can write down the amplitude condition within an integer multiple of 2π

$$r_1 r_2 e^{2(\Gamma g - \alpha)d} = 1. \tag{14}$$

Transforming equation (14), we get

$$\Gamma g_{\mathrm{th}} = \alpha + \frac{1}{2d} \ln \frac{1}{r_1 r_2} = \alpha + \alpha_{\mathrm{m}}, \tag{15}$$

where α_{m} describes mirror loss. This equation is the threshold condition. The phase condition is found as

$$\phi = 2d\beta = 2q\pi, \tag{16}$$

which can be rewritten as

$$q = 2nd/\lambda, \tag{17}$$

with q as an integer, n the index of refraction inside the cavity and λ the lasing wavelength. One can see that a resonance can only occur when an integer number of half-wavelengths fit into the cavity of length d.

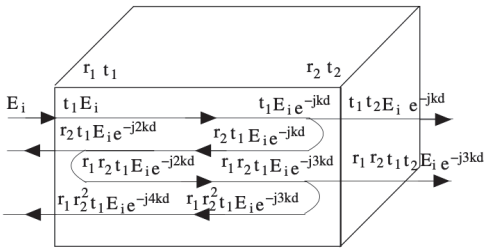

Figure 7: Electrical field propagation in a general Fabry-Perot resonator laser diode. Graphic taken from [61].

2.5 DBR Laser Diodes

After discussing the basic principles of diode lasers, we now want to take a look at state-of-the-art monolithic single-mode and wavelength tunable diode lasers. The Fabry-Perot cavity diode laser was discussed in the previous chapter. In order to achieve single-mode operation with wavelength tuning, the two-facet Fabry-Perot (FP) design needs to be modified. An approach to this is the cleaved-coupled-cavity diode laser (or C^3 laser), where a FP laser is split into two smaller FP lasers with unequal lengths. Between the two FP lasers, a third air-filled cavity is formed, which is typically a lot shorter than the two FP cavities surrounding it (<1 μm) [33] [32]. Besides having nice characteristics, these lasers are very hard to be manufactured and their stability during operation has shown to be problematic. The solution to single-mode and wavelength-tunable lasers are the Distributed Bragg Reflector (DBR) diode lasers and the Distributed Feedback (DFB) diode lasers.

In figure 8 (a) the schematic structure of a DFB laser is shown. Here, a grating is integrated in the active laser medium to produce distributed feedback over the total length of the laser resonator. One end is highly reflective (HR), whereas the output facet is of course built with a low reflectivity (LR) output coupler. The index of refraction in the active region has a spatially periodic distribution [61]

$$n(z) = n_0 + n_1 \sin\left(\frac{2q\pi z}{\Lambda} + \phi\right), \tag{18}$$

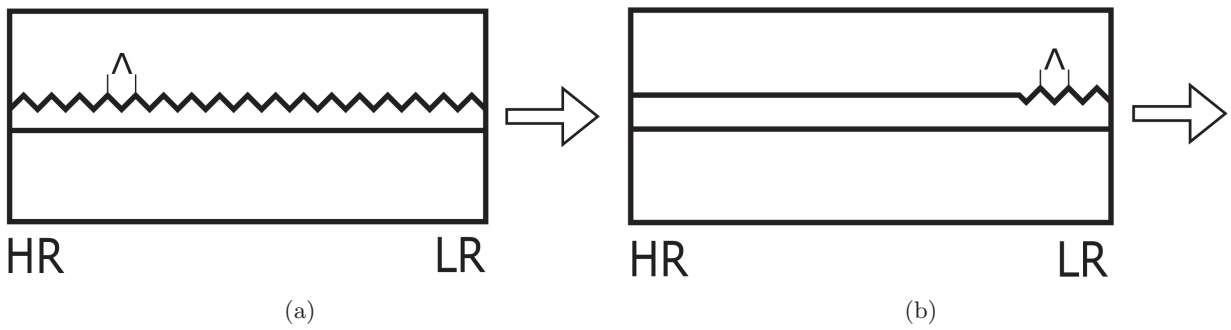

(a) (b)

Figure 8: Schematic structure of (a) a Distributed Feedback laser resonator and (b) a Distributed Bragg Reflector laser resonator. HR (LR) stands for high (low) reflectivity. The arrows indicate the light output direction.

with n_0 the refractive index of the medium without the grating (usually $n_0 >> n_1$), q an integer, z the coordinate along the propagation direction of light in the medium and Λ the pitch of the periodic thickness change. The forwards and backwards travelling beams in the DFB laser resonator can effectively couple to each other when the Bragg condition is fulfilled, namely for the first order $q = 1$

$$\lambda = \lambda_{\mathrm{B}} = 2n_0\Lambda. \tag{19}$$

So there are two ways to tune the wavelength: changing the refractive index or the pitch Λ in the medium. The main difference one can see in figure 8 (a) and (b) is that in a DFB laser diode, the grating is present over the whole length of the active medium, whereas in a DBR laser diode, the grating is separated from the active medium. This separated grating in a DBR laser diode is the so-called Bragg diffraction grating. Figure 9 shows the wavelength tunability of a typical DBR diode. The emission wavelength changes by either changing the injection current given to the diode or by altering the diode's temperature. When increasing the current, the emitted wavelength will undergo a red shift, which means longer wavelengths. This is mainly due to heating from the bigger current. A typical nubmer here is $0,002$ nm per mA [14]. This red shift is then continuous for some Δ_i, which is typically around $0,15$ nm. This is called the free spectral bandwidth. When we increase the current even more, the emitted wavelength will predictably undergo a blue-shift, essentially a mode hop. After this mode hop, the red shift with increasing current is retracing itself. When we stabilise our DBR diode in temperature, we are able to control the DBR diode's temperature as well as the injection current. A typical number for the influence of temperature on the wavelength is $0,074\ \frac{\mathrm{nm}}{\mathrm{K}}$ [14]. As can be seen in figure 9, it is possible to then tune the diode's wavelength to any value in it's range of operation.

2.6 External Cavity Diode Lasers

To improve the characteristics of a semiconductor laser diode, external cavity diode lasers have been developed. Compared to a normal laser diode, the external cavity allows for decreased noise and narrower linewidth of the diode chip as well as improved tunability [61, 40]. As has been mentioned before, the basic ingredients to build an ECDL are a diode laser, a collimator to couple the diode laser's output and some mode-selective element. In addition, one needs good electronic control over the diode laser for reliable operation. With this, one can apply optical feedback to the laser diode, which essentially extends the diode's laser resonator. The longer cavity increases the quality factor Q of the laser resonator and thus, the linewidth is narrowed and single-mode operation is stabilised. In this section, an introduction to two of the most common ECDL configurations is given.

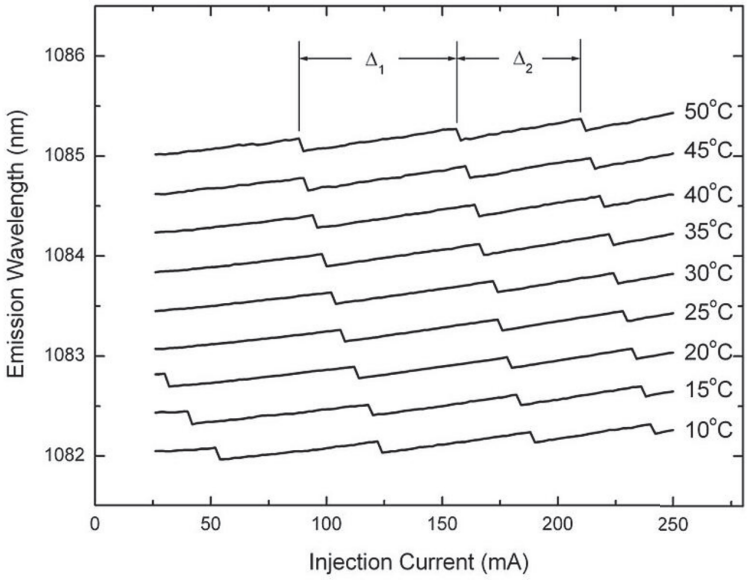

Figure 9: Emitted wavelength against the diode injection current for a typical DBR diode laser at different temperatures. Graphic taken from [14].

2.6.1 ECDL in Littrow Configuration

An ECDL in Littrow configuration utilises a grating as a mode-selective element. This grating can disperse the light spatially by it's wavelength. A typical layout of such an ECDL is shown in figure 10. In Littrow configuration, the angle of the incident beam on the grating and the angle of the outgoing beam from the grating are equal. Thus, the 0^{th} order beam is taken as the output beam, whereas the 1^{st} order reflected beam from the grating is used as the optical feedback to the diode laser. To get electronical control of the external cavity, a Piezo-electric transducer (PZT) is attached to the back of the grating and makes it possible to control the length of the external cavity and the wavelength. Tuning the wavelength is also possible by moving the grating. Usually, the grating is rotated, which changes the direction of the output beam. To overcome this, a mirror can be mounted perpendicular to the grating as it is shown in figure 10. This retro-reflector arrangement leaves the direction of the output beam unchanged when the grating is moved. However, some beam displacement is present when the axis of rotation is not chosen to be the intersection of the grating and the mirror. It has also been tested to increase the distance between the diode and the grating, thus making the external cavity even longer. But since this setup suffers from acoustic noise, making the external cavity too long is not practical. Littrow-design ECDL systems are easy to use, commercially available and not expensive. They also offer excellent performance, achieving linewidths on the order of 100s of kHz [43, 40, 45].

2.6.2 ECDL using a Confocal Fabry-Perot Cavity

An ECDL can also be built by using a confocal Fabry-Perot cavity (FPI) as the mode-selective element. The basic setup of such a laser system is shown in figure 11. A part of the laser diode's output light is sent to a FPI via a beam splitter. Optical feedback from the FPI can only take place, when the diode's wavelength matches the resonance condition of the FPI $2l = n\lambda$, with l being the length of the FPI, n the refractive index of the medium inside the FPI and λ the wavelength. Although the tunability of the laser is essentially the same as the bare diode laser, very narrow linewidths on the order of 10s of kHz can be achieved [36, 35]. Since the laser is locked relative to the FPI, the stability of the laser is also determined by the FPI. This can of course be an advantage

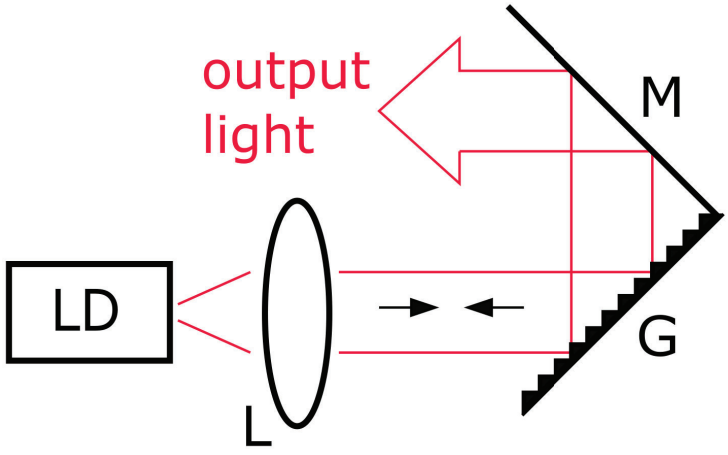

Figure 10: ECDL in Littrow configuration. The 1st order reflected beam from a grating (G) is used as optical feedback to the laser diode (LD). A mirror (M) attached to the grating makes sure, that the 0th order reflected beam from the grating does not change it's output direction when tuning the grating. The lens (L) is needed to collimate the beam.

or a disadvantage, depending on the intended use. Tuning the laser is done by electronic control of the FPI's length via a PZT on one of the FPI's mirrors (not shown in figure 11). A FPI is also affected by acoustic noise and temperature drifts in the environment, making it quite challenging to lock the laser to the FPI over long times.

There are of course many different variations of ECDL designs, all optimised to deliver the best performance for the intended use. To name a few important ones, there is the well-known Littman-Mettcalf ECDL configuration, the ring-cavity scheme and not long ago, we saw optical fibers being implemented in ECDL designs. In 2012 at MIT, a long-external cavity diode laser using an optical fiber in the optical feedback path was reported [51]. The schematic setup of this ECDL system is shown in figure 12 in the dashed rectangle. With the help of the optical fiber, the total cavity length could be extended to 3.6 m. They report a linewidth of about 300-400 kHz for the bare DBR diode, which then could be narrowed down to a minimum linewidth of 300 Hz.

A compact ECDL system using optical feedback from a fiber tip was reported in 2017 [53]. The small part of the light that gets reflected directly at the tip of an optical fiber is used as optical feedback, thus the cavity being formed from the reflective diode's rear facet up until the fiber tip. A linewidth of 50 kHz is reported with this technique.

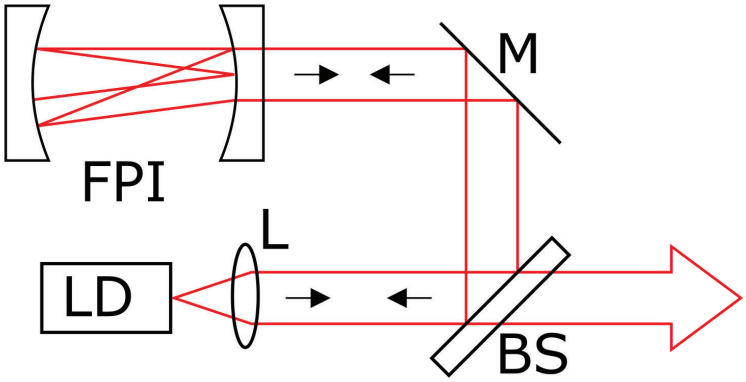

Figure 11: ECDL using a confocal FPI. Part of the light from a laser diode (LD) is sent to a confocal FPI via a beam splitter (BS), where optical feedback can only take place when the laser's wavelength matches the resonance of the FPI. M: mirror, L: lens for collimation.

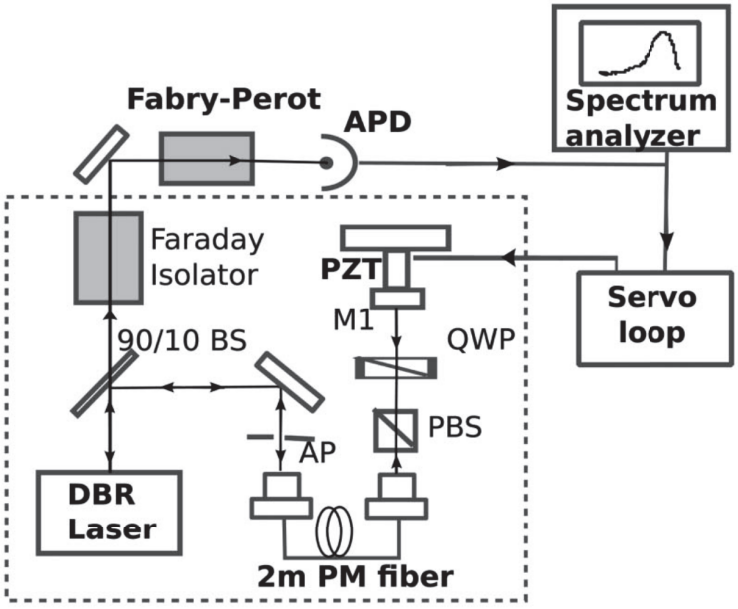

Figure 12: ECDL configuration using an optical fiber. BS: beam splitter, AP: aperture, PM fiber: polarisation maintaining fiber, PBS: polarising beam splitter, QWP: $\lambda/4$ waveplate, M1: mirror, PZT: piezo-electric transducer. Graphic taken from [51]

2.7 Laser Linewidth and Noise Spectral Density (NSD)

Two of the most important features of laser radiation is it's spatial and spectral coherence. While the spatial coherence is related to the divergence of a laser beam, the spectral coherence is determined by measuring the linewidth. This chapter concentrates on probably the most powerful feature of a ECDL: it's narrow linewidth.

2.7.1 Linewidth

A laser behaves similar to any other oscillator. The amplitude of the optical field stays nearly constant above laser threshold, but it's phase may take any value. The varying phase can be thought of as Brownian motion and has a big influence on the laser's linewidth [25]. These slow phase fluctuations are complemented by fast phase fluctuations, often called high-frequency noise

in this thesis. This high-frequency noise also adds to the linewidth of a laser, mostly shaping the wings of the laser line [34]. Schawlow and Townes derived a formula for the laser linewidth in their first paper presenting a laser [17], predicting that the product of the linewidth with the power $\Delta\nu P_0$ is constant. That would suggest, that the linewidth is narrowed inversely to the laser power. As it turns out, this is only valid below lasing threshold and some corrections have to be applied to the original formula. The modified Schawlow-Townes formula [24, 61]

$$\Delta\nu_q = \frac{h\nu_\mathrm{q} g n_\mathrm{sp} (\Delta\nu_\mathrm{g})^2}{P_0} \alpha_\mathrm{t} (1+\beta^2) \tag{20}$$

describes the full width at half maximum (FWHM) of the power spectrum of the electric field, which is a Lorentzian. P_0 is the power in the mode, h the Planck constant, ν_q the laser's frequency, n_sp the number of spontaneous emission photons in the mode, g the gain and α_t describes the total loss. For a solitary diode, the total losses read $\alpha_\mathrm{t} = \alpha - \ln\sqrt{R_1 R_2}$ and for a diode coupled to an external cavity $\alpha_\mathrm{t} = \alpha - \ln\sqrt{T^4 R_1 R_2}$, with R_1 and R_2 being the reflectivities of the two facets forming the laser resonator. The parameter β is the spectral linewidth enhancement factor with typical values from 2 to 8 [37]. $\Delta\nu_\mathrm{g}$ is the bandwidth of the Fabry-Perot cavity as a FWHM value. This parameter is connected to the photon lifetime τ_p, which again is connected to the single-pass cavity loss. It is found that [61]

$$\Delta\nu_\mathrm{gSD} = \frac{1}{2\pi\tau_\mathrm{p}} = \frac{c}{2\pi n d} \tag{21}$$

for a solitary diode laser, with n being the refractive index of the medium and d the length of the semiconductor medium. When a solitary diode laser is operated in an external cavity of length L, the photon lifetime τ_p increases due to the cavity being longer. The modified bandwidth for an external cavity laser is then found to be [61]

$$\Delta\nu_\mathrm{gEC} = \frac{c}{2\pi(nd+L)}. \tag{22}$$

If we compare the previous two equations 21 and 22, we see that

$$\Delta\nu_\mathrm{gSD} = \Delta\nu_\mathrm{gEC} \cdot (1+\gamma), \tag{23}$$

with $\gamma = \frac{L}{nd} \gg 1$. Thus, the spontaneous phase fluctuation limit to the linewidth is reduced in an external cavity diode laser compared to a solitary diode. Nevertheless, this relation only holds for low feedback (<1%). But since our laser has a total output power of around 50-60 mW depending on diode current and the optical feedback power in our laser is somewhere below 500μW, we are within this low feedback regime. Because of the longer cavity of an ECDL, which total length was described to be $nd + L$, the mode frequencies are now [61]

$$\nu_q = \frac{qc}{2(nd+L)}, \tag{24}$$

with $q = 1, 2, ...$ The strong dependence on the refractive index of the semiconductor is decoupled, due to the external cavity for $\gamma \gg 1$. For a solitary diode laser, the fluctuations of the semiconductor refractive index add to the laser linewidth significantly, but for an external-cavity laser they are negligible because the relative change in the mode frequency caused by the change in refractive index are reduced by the factor γ. To understand the influence of the external cavity length L on the linewidth, it is useful to rewrite equation 20 by the use of $g = -\ln(R)/(\eta L)$, where R again is the facet reflectivity and η is the quantum efficiency [31]:

$$\Delta\nu_q = \frac{(\Delta\nu_\mathrm{g})^2 n_\mathrm{sp} h\nu_q}{8\pi P_0 \eta L^2} \cdot \ln\left(\frac{1}{R}\right)^2 (1+\alpha^2). \tag{25}$$

For a fixed output power P_0, a long passive section in the cavity of length L decreases the spontaneous emission rate $n_\mathrm{sp} \propto L^{-1}$ and increase the average intensity $I \propto L$. This results in a reduction of the linewidth proportional to L^{-2} [34].

2.7.2 Noise Spectral Density (NSD)

We are using the Noise Spectral Density (NSD) of the error signal to determine the laser linewidth. In this chapter, a short description of the NSD is given, as well as how to calculate the linewidth out of it. The reader more interested in signal analysis theory may find [56, 57] useful. In general, a power spectral density $S_{xx}(f)$ of a time series $x(t)$ expresses the distribution of power of each frequency component of that time series. A PSD is called a NSD, when the signal of interest is a noise signal.

For a discrete-time signal $\{x(t); t = 0, \pm1, \pm2, ...\}$ we assume $x(t)$ to be a sequence of random variables

$$E\{x(t)\} = 0 \ \forall \ t, \tag{26}$$

having a zero mean value. $E\{\cdot\}$ is the expectation operator. It is used to define the covariance function $r(\tau)$ of $x(t)$ as [57]

$$r(\tau) = E\{x(t)x^*(t-\tau)\}. \tag{27}$$

It only depends on the delay between the two samples averaged and has some useful properties

$$r(\tau) = r^*(-\tau), \tag{28}$$

and

$$r(0) \geq |r(\tau)| \ \forall \ \tau. \tag{29}$$

A carried-out derivation of this can be found in [57].

With the covariance function (27), the power spectral density (PSD) is defined as [57]

$$S(\omega) = \sum_{k=-\infty}^{\infty} r(\tau)e^{-i\omega\tau}. \tag{30}$$

We now want to bring this very general definition of the PSD into relation with our experiment and the laser's linewidth. First, we need to consider a covariance function described by a real signal we are detecting with a photodiode. This signal is of the form

$$V_{\mathrm{L}}(t) = V_0 e^{i[\omega_0 t + \phi(t)]}, \tag{31}$$

in units of Volts. ω_0 is the center frequency, $\phi(t)$ is a phase and the subscript L denotes its relation to our laser. With this, we can then write down the autocorrelation function (there is no difference between a covariance function and an autocorrelation function in this case, since the time and ensemble averages are equal) [30]

$$r_{\mathrm{L}}(\tau) = \frac{1}{2}\Re \lim_{T\to\infty} \frac{1}{T} \int_{-\frac{T}{2}}^{\frac{T}{2}} V_{\mathrm{L}}(t)V_{\mathrm{L}}^*(t+\tau)dt \tag{32}$$

$$= \frac{1}{2}\langle V_{\mathrm{L}}(t)V_{\mathrm{L}}^*(t+\tau)\rangle \tag{33}$$

$$= \frac{V_0^2}{2}\cos(\omega_0\tau)\exp\{-\frac{1}{2}\langle[\phi(t)-\phi(t+\tau)]^2\rangle\}. \tag{34}$$

To bring the autocorrelation function in relation with the power spectral density $S(f)$, the Wiener-Khintchine Theorem is used:

$$S_{\mathrm{V}}(f) = 4\int_0^{\infty} r_{\mathrm{L}}(t)\cos(\omega t)dt. \tag{35}$$

This Fourier Transform integral now relates the autocorrelation function with the PSD $S_{\mathrm{V}}(f)$, which has units of $\frac{\mathrm{V}}{\sqrt{\mathrm{Hz}}}$. To determine the laser linewidth in units of Hz, $S_{\mathrm{V}}(f)$ needs to be transformed

into a PSD $S_\nu(f)$ in terms of the laser frequency ν. This can be done by independently measuring the error signal and determining it's slope s in units of $\frac{\mathrm{Hz}}{\mathrm{V}}$. To transform the PSD in terms of V into a PSD in terms of the laser frequency ν, we simply multiply $S_\mathrm{V}(f)$ with the error signal slope:

$$S_\nu(f) = S_\mathrm{V}(f) \cdot s. \tag{36}$$

To clarify this, we perform the equation above just with the units:

$$\frac{\mathrm{Hz}}{\sqrt{\mathrm{Hz}}} = \frac{\mathrm{V}}{\sqrt{\mathrm{Hz}}} \cdot \frac{\mathrm{Hz}}{\mathrm{V}}. \tag{37}$$

If we now look at a typical NSD of a DBR diode laser (see figure 13, it becomes clear that at high noise frequencies, $S_\nu(f)$ basically has some constant value S_0 and is independent of frequency. We then can estimate the laser linewidth $\Delta\nu$ by using [51]

$$\Delta\nu = \pi S_0^2. \tag{38}$$

Another, more accurate way to calculate the laser linewidth is provided in [53], where the relation is originally found in [38]:

$$\int_{\Delta\nu}^{\infty} \frac{S_\nu^2(f)}{f^2} df = \frac{1}{\pi}. \tag{39}$$

This can also be used to calculate the laser linewidth and takes into account small deviations from the constant value S_0 used in equation (38). Note, that the latter equation uses the power spectrum S_ν^2, and not the power spectral density S_ν. In this thesis, equation (39) is used throughout to determine $\Delta\nu$.

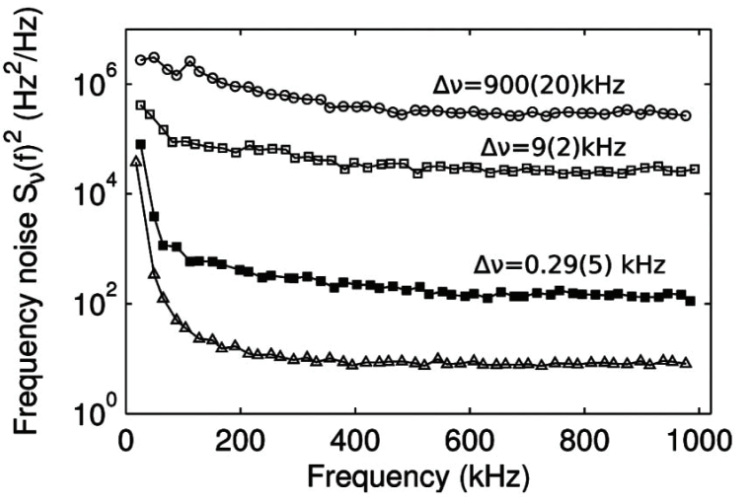

Figure 13: NSDs for different setups. From top to bottom: bare DBR diode laser, short ECDL, long ECDL, measurement noise floor. Graphic taken from [51]

2.8 Cesium

We are using a Cesium (Cs) vapour cell at room temperature to get an error signal for laser-locking via the technique described in the next section. But first let us take a closer look at the Cs atom and some of it's properties. Cesium is an Alkali-metal with the atomic number of 55. It can be found in the s-block of the periodic table. With only one electron in it's outermost shell, Cs has very similar chemical and physical properties to Rubidium and Potassium. Cs was originally

discovered by Robert Bunsen and Gustav Kirchhoff in 1860 [15]. Then in 1955, a report in Nature [16] suggested a higher accuracy in the definition of the second with the Cs atom. At that time, the quartz standard defined the second. From 1967 on, Cs was used by the International System of Units to define the second by the emission spectrum of ^{133}Cs [26], the only stable isotope of Cs. Besides defining the second, Cs is also relevant in quantum optics experiments and in our case, the Cs D2 line is used as an absolute reference for laser-locking. The energy level scheme of ^{133}Cs is shown in figure 14. Note that the hyperfine splitting in the ground state $6^2S_{1/2}$ $F = 3 \rightarrow F = 4$ is given as an exact value of $2\pi\cdot$9,192631770 GHz (in absence of external influences; e.g. Earth's magnetic field,...). This is because the second is defined by this hyperfine transition. The D2-line we are using in our laser system is the transition from $6^2S_{1/2}$ $F = 4 \rightarrow 6^2P_{3/2}$ $F = 5$, with a frequency splitting of $2\pi\cdot$351,721 933 533 (111) THz (calculated using data from figure 14). This transition is a so-called closed transition, meaning the atom cannot relax into other ground states but the $F = 4$ hyperfine level, due to selection rules. We will further denote the Cs D2-transition as $F = 4 \rightarrow F' = 5$.

2.9 Modulation Transfer Spectroscopy (MTS)

Active frequency stabilisation of a laser system, also known as *locking* of a laser, plays an important role in many atomic physics experiments and particularly when one wants to perform laser cooling. There are many techniques to generate a so-called error signal which can be used to stabilise a laser's frequency, such as dichroic atomic vapour laser lock (DAVLL) [48], [41], saturation absorption spectroscopy [39], Sagnac interferometry [47], polarisation spectroscopy [29], [46], frequency modulation (FM) spectroscopy [59] and modulation transfer spectroscopy (MTS) [49], [52]. One needs to differentiate between single-beam techniques, such as DAVLL for example, and techniques using two laser beams. These single-beam techniques show Doppler-broadened spectral features, therefore delivering shallower signal gradients capturing a range of several hundred MHz. Pump-probe techniques on the other hand achieve sub-Doppler resolution and much steeper signal gradients within a capture range of typically below one hundred MHz. Thus, pump-probe error signals are better suited to be used for laser locking.

Now let us have a look at how MTS works: We need two counter-propagating laser beams travelling through some atomic vapour. In addition to that, one of the beams needs to be modulated with e.g. an Electro-Optic Modulator (EOM). The modulated beam will be called the pump beam and the counter-propagating beam the probe beam. An important difference to, for instance, saturation absorption spectroscopy is, that the powers of both beams should be approximately equal in the case of MTS. The single-frequency pump beam is sent through an EOM, which is driven by some oscillator at a modulation frequency ω_m. The transmitted beam is now phase-modulated and shows a carrier wave at frequency ω_c and two sidebands at frequencies $\omega_\mathrm{c} \pm \omega_\mathrm{m}$. Note that we only take into account the first order sidebands. This can be done because usually one uses a modulation index $\delta < 1$, which modulates the probe beam in a way that it has a strong carrier wave ω_c and two weak sidebands $\omega_\mathrm{c} \pm \omega_\mathrm{m}$, whereas higher order sidebands are negligible. If we write down the equation for the phase-modulated pump beam, we get [49]

$$E = E_0 \sin\big[\omega_\mathrm{c} t) + \delta \sin(\omega_\mathrm{m} t)\big], \tag{40}$$

$$E = E_0\Big[\sum_{n=0}^{\infty} J_n(\delta)\sin(\omega_\mathrm{c} + n\omega_\mathrm{m})t + \sum_{n=1}^{\infty}(-1)^n J_n(\delta)\sin(\omega_\mathrm{c} - n\omega_\mathrm{m})t\Big]. \tag{41}$$

Here $J_n(\delta)$ is the Bessel function of order n and δ is the modulation index. Furthermore, E_0 describes the electric field amplitude and t denotes the time. After the pump beam is modulated, the pump and probe beams are aligned collinearly through a vapour cell. If the laser's carrier frequency is resonant with an atomic transition, modulation transfer can take place. Two frequency components

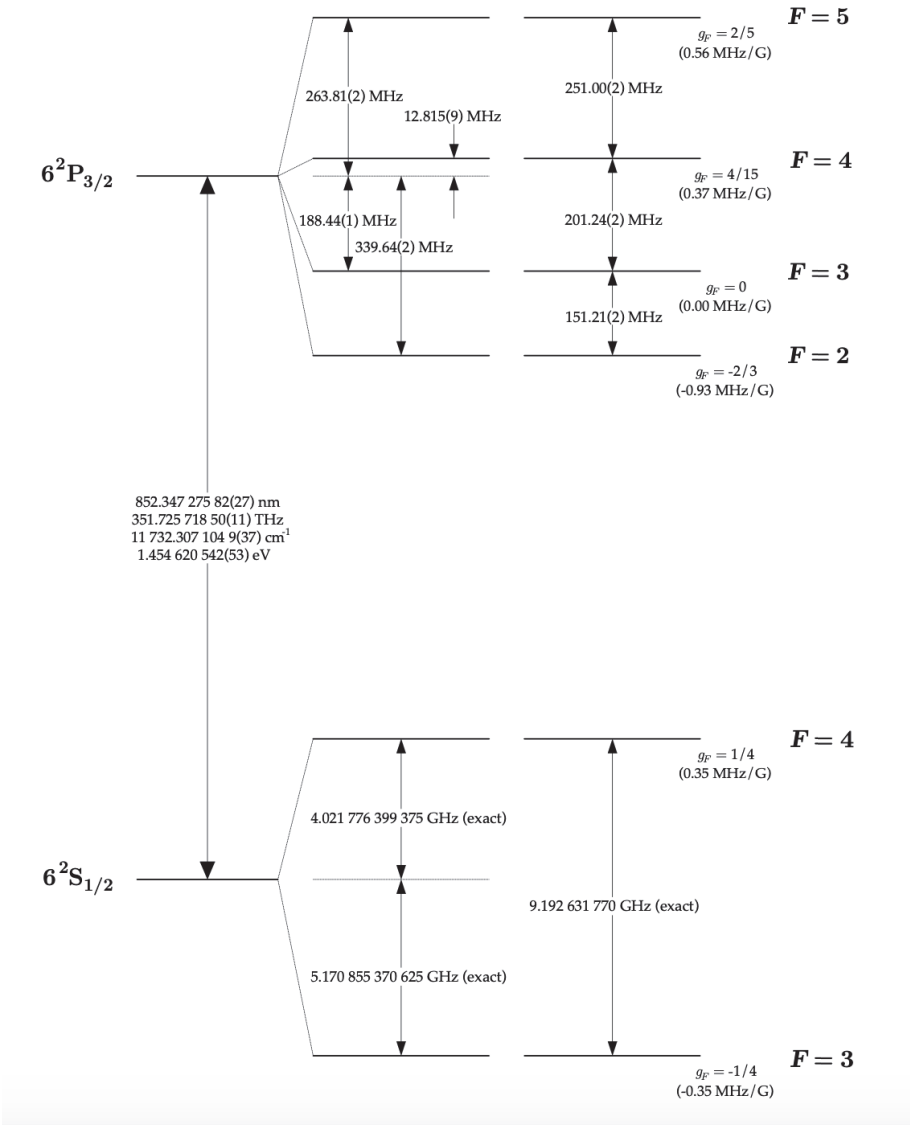

Figure 14: Cesium energy level scheme. The frequency splittings between the hyperfine energy levels are shown. Graphic taken from [50].

of the pump beam, the carrier ω_c and one sideband $\omega_c \pm \omega_m$ combine with the counter-propagating probe beam. With the non-linearity (third order susceptibility $\chi^{(3)}$) of the absorbing medium (the atomic vapour), a fourth wave is generated, which is a sideband on the probe beam. This happens for both the sidebands of the pump beam, so that the modulation of the pump beam is transferred to the probe beam. Note that this process can only occur when the sub-Doppler resonance condition is fulfilled. This four-wave mixing process is the most efficient for closed atomic transition, where the atoms in the atomic vapour can only relax to one specific initial state. This is a great advantage as we are using the closed transition $F = 4 \rightarrow F' = 5$ in Cs, as already described in section 2.8. Other advantages of MTS are a flat and zero background signal, which makes the baseline of the lineshape independent from changes in absorption coming from intensity-, polarisation- or temperature-fluctuations in the laser beam. Furthermore, the position of the zero-crossing always marks the centre of the sub-Doppler resonance. After the vapour cell the probe beam hits a photo detector, which detects a signal of the form ([49], [60])

$$S(\omega_m) = \frac{C}{\sqrt{\Gamma^2 + \omega_m^2}} \sum_{n=-\infty}^{\infty} J_n(\delta) J_{n-1}(\delta) \tag{42}$$

$$\cdot \Big[(L_{(n+1)/2} + L_{(n-2)/2} \cos(\omega_m t + \phi) \tag{43}$$

$$+ (D_{(n+1)/2} + D_{(n-2)/2} \sin(\omega_m t + \phi) \Big], \tag{44}$$

with

$$L_n = \frac{\Gamma^2}{\Gamma^2 + (\Delta - n\omega_m)^2} \tag{45}$$

and

$$D_n = \frac{\Gamma(\Delta - n\omega_m)}{\Gamma^2 + (\Delta - n\omega_m)^2}, \tag{46}$$

where Δ is the frequency detuning from the line centre, ϕ is the detector phase, Γ is the natural linewidth and C represents all properties of the medium and the probe beam which are not described by the other parameters. When we remember to best use small modulation indices $\delta < 1$, we can only consider the first order sidebands and equation (42) simplifies to

$$S(\omega_m) = \frac{C}{\sqrt{\Gamma^2 + \omega_m^2}} J_0(\delta) J_1(\delta) \tag{47}$$

$$\cdot \Big[(L_{-1} - L_{-1/2} + L_{1/2} - L_1) \cos(\omega_m t + \phi) \tag{48}$$

$$+ (D_1 - D_{1/2} - D_{-1/2} + D_{-1}) \sin(\omega_m t + \phi) \Big]. \tag{49}$$

In equations (42) and (47) one can see a sine term and a cosine term each, where the sine term represents the quadrature component of the signal and the cosine term the in-phase component. Thus it is possible to select either one of these components with a phase-sensitive detection scheme to get either the absorption or the dispersion components. In figure 15 theoretical MTS signals are shown for the in-phase and quadrature components. We see that both signals from (a) and (b) of figure 15 have a large gradient occurring on the centre of the resonance. Furthermore, given that $\omega_m \leq \Gamma$, both the in-phase and quadrature signals have a similar line-shape. Thus they can be used as 'error signals' for laser locking.

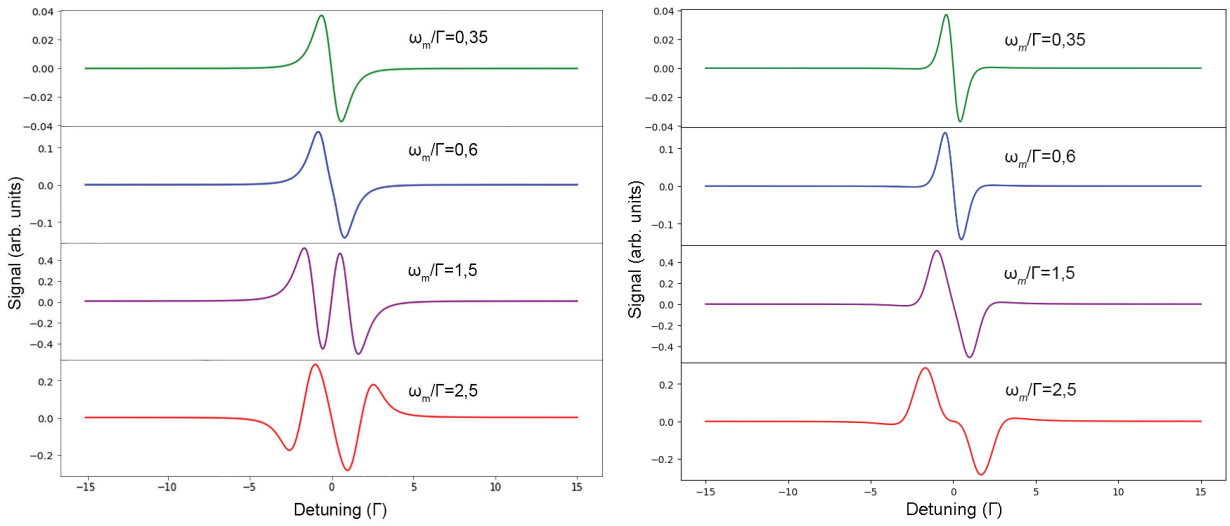

(a) (b)

Figure 15: Theoretical MTS signals. Modulation frequencies are denoted in the figure. (a) In-phase component - cosine term of equations (42) and (47); (b) Quadrature component - sine term of equations (42) and (47).

2.10 Coupling of Laser Light into a Single-Mode Optical Fiber

Optical fibers are a special class of waveguides. With the principle of total internal reflection, light is guided through the core of an optical fiber. Today, optical fibers are used in many different applications such as telecommunication, spectroscopy and sensor and measurement technology to name a few. In figure 16 a schematic view on an optical fiber is shown. A plastic coating forms the outermost shell of the fiber cable and is needed to protect the cladding and the core of the optical fiber. The core is typically made of silica with some dopants in it to modify the refractive index n of the material so that $n_1 > n_2$. In particular, we are working with so-called step-index fibers. These have $n_1 = \text{const.}$ in the core and the refractive index steps down to n_2 in the cladding. In contrast to step-index fibers, there are the gradient-index fibers where the refractive index n_1 in the core gradually approaches n_2 in the cladding without any step in refractive index. We will continue the discussion with the step-index fiber shown in figure 17. In order to achieve total inner reflection in the fiber core, the incoming laser light has to hit the center of the fiber core within some maximum entrance angle, denoted α_{max}. We can use Snell's law to calculate the critical angle α_{crit} for total inner reflection.

$$\sin(\alpha)n_1 = \sin(\alpha')n_2, \tag{50}$$

where α is some angle of the light inside the fiber core incident on the core/cladding boundary and α' is the angle of the light refracted into the fiber cladding. Since $\sin\alpha'$ cannot get bigger than 1, we get the condition

$$\sin(\alpha) \leq \frac{n_2}{n_1}, \tag{51}$$

describing the angles at which light enters the cladding. Thus, the critical angle for total inner reflection is

$$\sin(\alpha_{\text{crit}}) = \frac{n_2}{n_1}, \tag{52}$$

and all the light with $\sin(\alpha) > \frac{n_2}{n_1}$ is totally reflected inside the fiber core. Now the angle of maximum acceptance α_{max} can be calculated

$$n\sin(\alpha_{\text{max}}) = n_1\sin(\alpha_{\text{t}}) = n_1\sqrt{1-\cos^2(\alpha_{\text{t}})}, \tag{53}$$

where $n = 1$ is the refractive index outside the fiber core. With the help of

$$\sin(\alpha_{\text{crit}}) = \frac{n_2}{n_1} = \cos(\alpha_{\text{t}}), \tag{54}$$

we can write

$$\sin(\alpha_{\text{max}}) = \sqrt{n_1^2 - n_2^2}, \tag{55}$$

which is, per definition, the numerical aperture NA $= \sin(\alpha_{\text{max}}) = \sqrt{n_1^2 - n_2^2}$ of an optical fiber [55]. There are step-index fibers with a large core diameter of about 100-500 μm, these are typically multimode fibers because the large core diameter allows the propagation of higher order modes. In our experiment, we are using single-mode step-index fibers, with a core that is much smaller in it's diameter (around 2-10 μm). Because of that, the coupling of laser light to such a single-mode fiber needs to be more accurate. The numerical aperture of an optical fiber is given by the manufacturer. So if we measure the diameter d of our laser beam, we can calculate the focal length f to choose the correct lens for our specific setup. Using

$$2\alpha_{\text{max}} f = d, \tag{56}$$

and

$$\text{NA} = n \sin(\alpha_{\text{max}}) \approx n\alpha_{\text{max}}, \tag{57}$$

we end up with the expression

$$f = \frac{d}{2\frac{\text{NA}}{n}} \tag{58}$$

to calculate the focal length needed to maximise the coupling efficiency of laser light into the optical fiber.

Since the fiber core of a single-mode fiber has a very small diameter of around 2-10 μm, we need to be able to focus the laser beam exactly into the fiber core. The focusing part is done by the correct lens chosen by equation 58. The part of actually hitting the fiber core with the focused beam is usually done with a setup similar to the one shown in figure 21. Two moveable stages with $X-$ and $Y-$adjustment screws each are needed, meaning we have in total four degrees of freedom to adjust the direction of the laser beam. Laser light is coupled to an optical fiber efficiently, when the incoming beam to the fiber port is overlapping with an imaginary beam exiting the fiber and counterpropagating the incoming beam. With the fiber port and the mirror on the PZT on moveable stages, we can adjust both stages in a way that the two beams overlap at the fiber port and in front of the mirror. This technique is also used widely in the labs, where for the imaginary counterpropagating beam, a laser pointer is used that can be attached to the end of a fiber directly. In the following section, the principle of a Risley prism scanner is described and how it can be used to eliminate these moveable stages needed for fiber coupling.

2.11 Risley Prism Scanner

In section 3.1.2 we will replace the movable stages in the ECDL setup with two Risley prism pairs to steer the beam into the optical fiber and to eliminate moveable elements with springs in the setup. In this section, the theory of operation for such a Risley prism scanner is described.

Let us first consider only a single wedge prism like it is shown in figure 18. We are using round wedge prisms that have one flat side and one wedged side, which is wedged at some angle α. We can use Snell's law to determine the angle at which the wedged side of the prism refracts the incoming light:

$$\sin(\phi_i) = n_g \sin(\phi_p) \Leftrightarrow \sin(\phi_p) = \frac{\sin(\phi_i)}{n_g}, \tag{59}$$

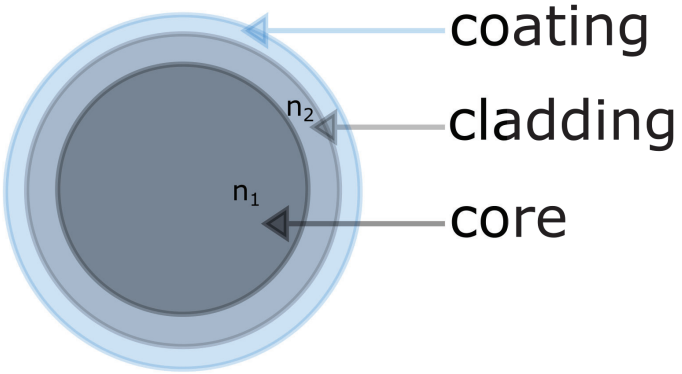

Figure 16: Schematic view on an optical fiber. The refractive index of the core n_1 is bigger than the refractive index of the cladding n_2 to allow for total inner reflection.

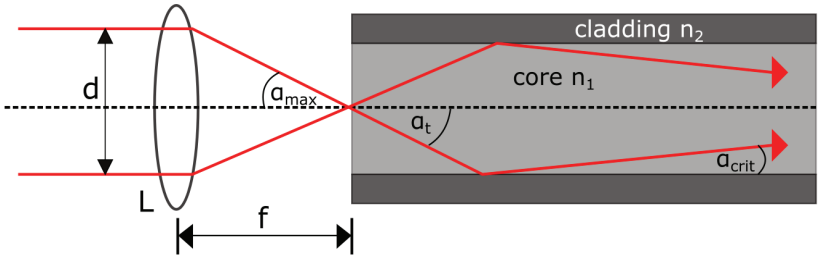

Figure 17: Cross section of a step-index fiber. To couple light efficiently into an optical fiber, the focal length f of the lens (L) needs to be chosen correctly for different laser beams with diameter d and different numerical apertures of the fiber.

where we have already used $n = 1$ for outside the prism. Since our wedge prisms used have a $\alpha < 10°$, we can apply the small-angle approximation to our expression and get $\phi_p = \phi_i/n_g$. To determine the output angle ϕ_o, we need to apply once again Snell's law, but this time for the second flat face. The angle of the light incident on the flat surface is $\phi_i - \phi_p$ and the refractive index outside the prism is again $n = 1$, so

$$n_g \sin(\phi_i - \phi_p) = \sin(\phi_o). \tag{60}$$

Applying again the small-angle approximation and inserting $\phi_p = \phi_i/n_g$ from above, we get

$$n_g(\phi_i - \frac{\phi_i}{n_g}) = \phi_o \Leftrightarrow \phi_o = \phi_i(n_g - 1). \tag{61}$$

It is to note that this result for the angle of the outgoing beam ϕ_o is the same for when the light is incident on the wedged or the flat surface of the prism first, but to be exact only in the small-angle approximation. In figure 18 we can see an angle $\theta = 90°$. This will from now on be referred to as the initial position of the prism with its thickest part on the top. The angle θ describes the rotation of the prism along the z-axis (coordinate system shown in figure 18). If we were to rotate the prism a whole turn, the beam would mark out a circle with radius r' on a screen at a distance S. We will give the expressions for the radius without the derivation here. The more interested reader may find additional information on the derivation in [12]. The radius r' in figure 18 is found to be [12]

$$r' = r_S + r_T = S\tan(\phi_o) + T\tan(\phi_i - \phi_p), \tag{62}$$

where $T = T_{max} - \frac{1}{2}D\tan(\alpha)$ is the thickness of the prism in the middle, T_{max} is the maximum thickness of the prism and D is it's diameter. With this, we can write down the equations that

describe the beam's position after a single wedge prism [12]

$$x(\theta) = r' \cos(\theta),\ y(\theta) = r' \sin(\theta). \tag{63}$$

Now we can expand these results to the situation where we have 2 wedged prisms close together like it is shown in figure 19. Figure 19 shows the configuration where both wedge prisms are oriented at $\theta_1 = \theta_2 = 90°$ for prism 1 and 2 respectively. In this position, the maximum radius r_{max} is reached. The figure also shows, that the path through the second prism $T+T'$ is larger than the path through the first prism T. The distance T' is dependent on r', namely how much lateral displacement of the beam is added by the first prism, and $|\theta_1 - \theta_2|$, the difference of rotation of each prism. The distance T' can be calculated using [12]

$$T' = r' \tan(\phi_i) \cos(|\theta_1 - \theta_2|). \tag{64}$$

If we imagine that prism one traces out a circle at r_1, then the second prism adds to that radius the radius r_2. For some distance z, we then have

$$r_r = r_1 + r_2 = z \tan(\phi_o) + z \tan(\phi_o) = 2z \tan(\phi_o). \tag{65}$$

The smallest possible radius for the system of two wedged prisms is found to be

$$r_d = (2T + T') \tan(\phi_i - \phi_p) + S \tan(\phi_o), \tag{66}$$

and the maximum radius of the system is then [12]

$$r_{max} = r_d + r_r \approx (2T + T') \tan(\phi_i - \phi_p) + (2z + S) \tan(\phi_o). \tag{67}$$

So a Risley prism scanner can point a laser beam anywhere on the annulus created by r_{max} and r_d. To understand, why the beam cannot point inside r_d, see figure 20: although the contributions of both prisms result in a beam path that is parallel to the original beam path, it is still offset by r_d, this is also called center defect. Since the contributions of each prism are additive, we can again create a set of equations to describe the beam's position after going through a Risley prism scanner [12]:

$$x(\theta_1, \theta_2) = (r_1 + r_d) \cos(\theta_1) + r_2 \cos(\theta_2), \tag{68}$$
$$y(\theta_1, \theta_2) = (r_1 + r_d) \sin(\theta_1) + r_2 \sin(\theta_2). \tag{69}$$

In our experiment, we will use two Risley prism pairs to replace two moveable stages in the ECDL setup to couple the laser light into the optical fiber only using two pairs of Risley prisms.

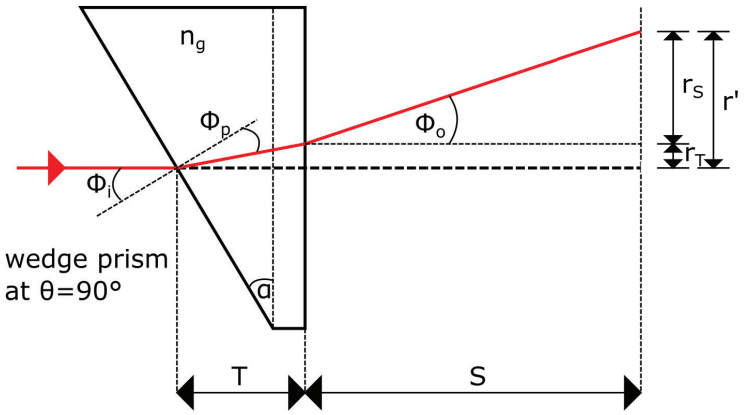

Figure 18: A single wedge prism with it's thickest part aligned to the top of the page. The beam path of a monochromatic beam is shown.

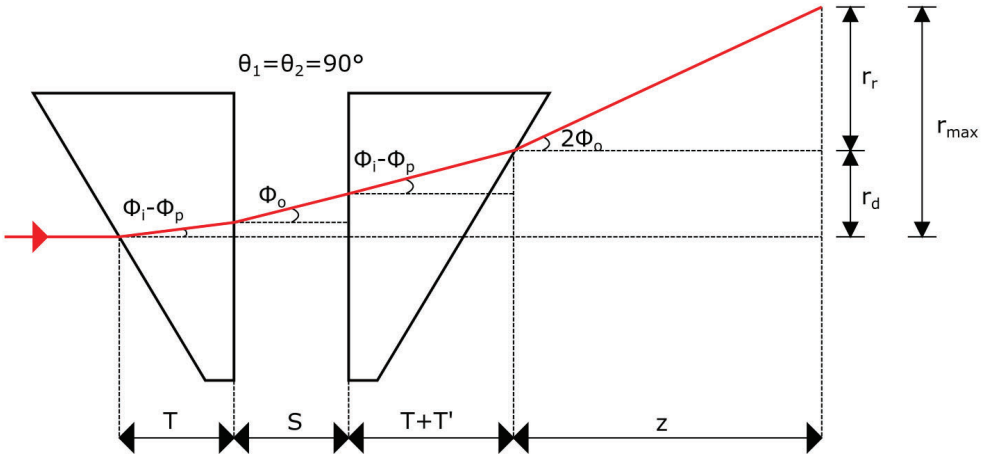

Figure 19: When both wedge prisms are rotated to the same position in θ, the outgoing beam reaches the maximum displacement.

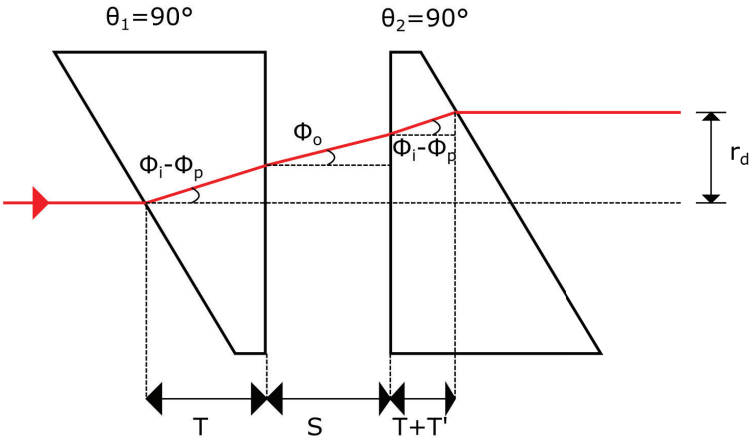

Figure 20: When the wedge prisms are offset by 180°, the minimum displacement of the beam is reached, where r_d is indicating the forbidden area where the beam cannot be pointed to (center defect).

3 Experimental Setup

3.1 Optical Setup

In this section, the optical setup of the experiment is described. The goal is to build an ECDL laser system with the use of an optical fiber in the optical feedback path of the ECDL. This has already been done before [51], but as far as we know only with a setup like in figure 12, where the beam needs to enter the optical fiber two times. Since we know how sensitive fiber coupling is, we assume it would be way easier if the laser beam does not have to enter the optical fiber twice. This is why we are using a retro-reflecting optical fiber, where the beam enters the fiber once and is back-reflected inside the fiber itself. In addition, using an optical fiber of this kind makes it easier to align the setup. In the following section 3.1.1, the first ECDL setup is introduced, where we use classical spring-loaded moveable stages for the fiber port and the mirror on the piezoelectric transducer. In section 3.1.2, the second ECDL setup is described where we want to renounce on the moveable stages and have every optical element fixed and free from mechanical springs. The spectroscopy branch where MTS is performed, stayed the same in both cases and is described in section 3.1.2.

3.1.1 First ECDL Setup with Movable Mirror Mounts

We started this experiment by designing an ECDL setup that could include the retroreflecting optical fiber and was fast and easy to adjust and couple light into the optical fiber. This is shown as a schematic sketch in figure 21 and as a photograph in figure 22. A DBR diode laser (SDL-5712-H1) at 852 nm is mounted on a ThorLabs laser diode mount with a lens cage-mounted in front of it [6]. This lens is used to collimate the outgoing beam. The DBR diode and the collimation lens are mounted inside a small housing to protect the diode and the electronics from the environment. As we know from section 2.4, the emitted laser light from the bare diode has an elliptical shape. Thus, in addition to the collimation lens, a prism pair (manufacturer/modelname unknown) directly after the collimation lens is used to expand the smaller axis of the ellipse to shape the beam circular. A $\lambda/2$ and a PBS is then used to split the laser beam into a strong outgoing beam and a weak beam for optical feedback. To couple the laser light into a 1 m long ThorLabs retro-reflecting and polarisation maintaining optical fiber P5-780PMR-P01-1 [10], we use a mirror glued to a piezoelectric transducer (PZT, manufacturer/modelname unknown), which is mounted to a standard movable mirror mount. Also the fiber port is mounted on a movable stage, as can be seen in figure 22. This gives us the necessary degrees of freedom to easily couple the light into the optical fiber. This fiber port also holds a ThorLabs C220TM-B [3] aspheric lens to focus the laser beam into the core of the optical fiber. The $\lambda/2$ in combination with another PBS after the PZT is used to further adjust the power of the laser light in the extended cavity. An additional $\lambda/2$ acts as a polarisation filter, to only send light into the optical fiber that matches the polarisation of it. For the characterisation of this setup, see section 4.2.

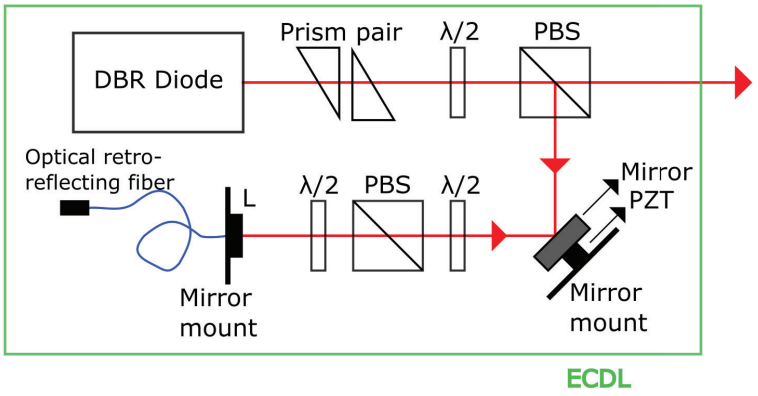

Figure 21: Optical setup of the first ECDL design: After collimation, the beam splits up at the PBS in combination with a $\lambda/2$ into a strong outgoing beam, exiting the green rectangle to the right, and a weak beam for optical feedback in the ECDL path. A mirror glued to a piezoelectric transducer (PZT) on a moveable stage is used in combination with a moveable stage for the fiber port to couple the light into the retro-reflecting optical fiber with a lens L. The second $\lambda/2$ in combination with the PBS is used to further adjust the power in the ECDL and the third $\lambda/2$ is used to match the polarisation of the light to the polarisation maintaining retro-reflecting optical fiber.

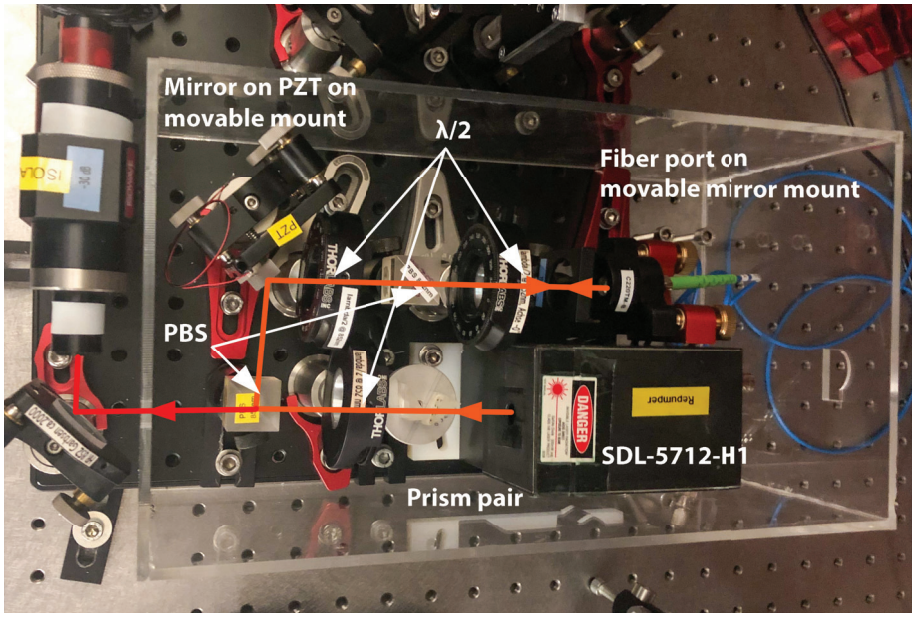

Figure 22: Photo of the ECDL setup with the mirror glued to the PZT on a moveable stage and the optical fiber port also on a moveable stage. The laser diode SDL-5712-H1 with the collimation lens is situated inside the black housing on the top right corner of the picture. The plexi-glass housing shown here is also the first prototype for the aluminium housing shown in the following section. The ECDL beam path is shown in orange, where the red beam path indicates the output beam. On the left of the photo outside the plexi-glass box, the output beam is guided through the optical isolator and further to the MTS branch.

3.1.2 ECDL Setup with two Risley Prism Pairs

After doing some measurements for the laser linewidth with the first ECDL setup, we thought about what could be improved to further narrow the laser's linewidth. The idea was to eliminate all moveable parts, since we believe that the springs in the mirror-mount and the fiber mount introduced acoustic noise and mechanical vibrations from the environment on top of the laser. In the new ECDL setup, which can be seen as a schematic sketch in the top green rectangle in figure 23, the same DBR laser diode at 852 nm (SDL-5712-H1) is mounted on the same ThorLabs laser diode mount with a lens cage-mounted in front of the diode [6]. But this time, the laser diode and lens mount are bolted on a custom built Aluminium base plate, which can hold all of the ECDL setup that is shown in the green rectangle. A photo of this is shown in figure 24. This base plate can then be closed with a separate top-part after alignment to isolate all the optical elements in the ECDL setup from the environment. We also went from one-inch optics to half-inch optics to shrink the size of the whole setup. Since the beam has an elliptical profile after exiting the laser diode and collimation lens, the same prism pair is used to expand the smaller axis of the ellipse to achieve a round beam profile. A $\lambda/2$ waveplate is used in combination with a Polarising Beam Splitter (PBS) to create a high-power outgoing beam and a low-power beam to feed the optical resonator. The external cavity consists of the same ThorLabs P5-780PMR-P01-1 retro-reflecting and polarisation maintaining optical fiber [10], which is mounted to a static fiber mount. Again this static fiber mount also holds the ThorLabs C220TM-B [3] lens for fiber coupling. Via two Risley Prism pairs (Edmund Optics 2 deg wedge prism VIS-NIR [1] mounted on a ThorLabs high precision rotation mount PRM05/M [11]), the beam is steered into the optical fiber. A mirror glued to a tubular Piezo transducer (manufacturer/modelname unknown) is attached on a static mount. This Piezo is used to electronically control the cavity length for laser locking. Another $\lambda/2$ and a PBS after the second Risley prism pair is again used to further adjust the power of the beam. Also, the last $\lambda/2$ in front of the fiber mount is again used to match the polarisation of the light to the polarisation maintaining optical fiber. This whole ECDL setup is placed into a custom-built Aluminium box to make it nice and compact and of course to reduce environmental effects such as acoustic waves or air blasts. The effectiveness of this Aluminium laser housing will be investigated during the course of this thesis. Furthermore, it is to note, that all optical elements are attached to static mounts without any springs in use. The rotatable prisms and $\lambda/2$ waveplates can be fixed by tightening a bolt.

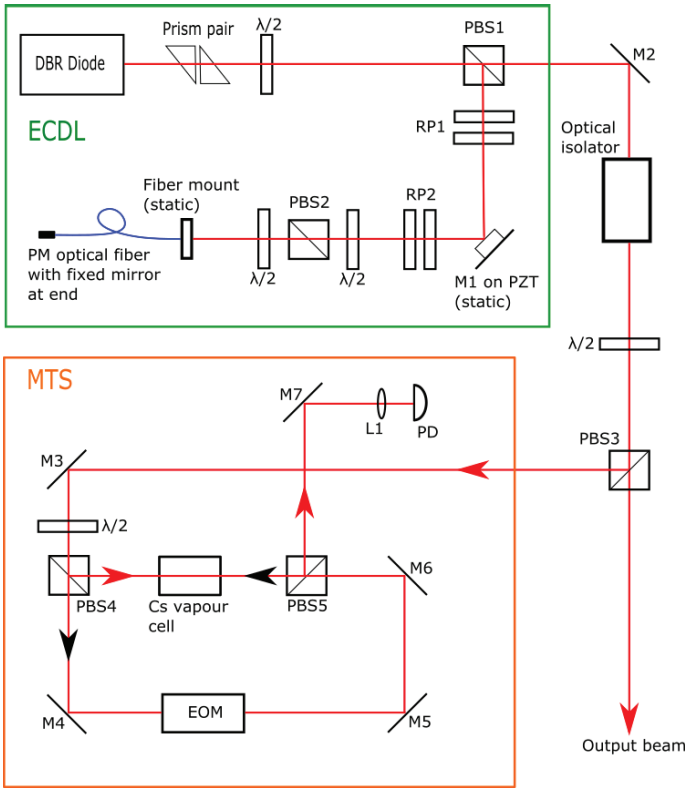

Figure 23: Optical setup: In the top rectangle (green) the ECDL setup is shown. All of these components are placed into a custom-made aluminium box to ensure isolation from the environment. In the bottom rectangle (orange) the MTS setup is shown. PBS - polarising beam splitter; M - mirror; RP - Risley prism pair; PZT - tubular Piezo transducer; L - lens; PD - photodiode.

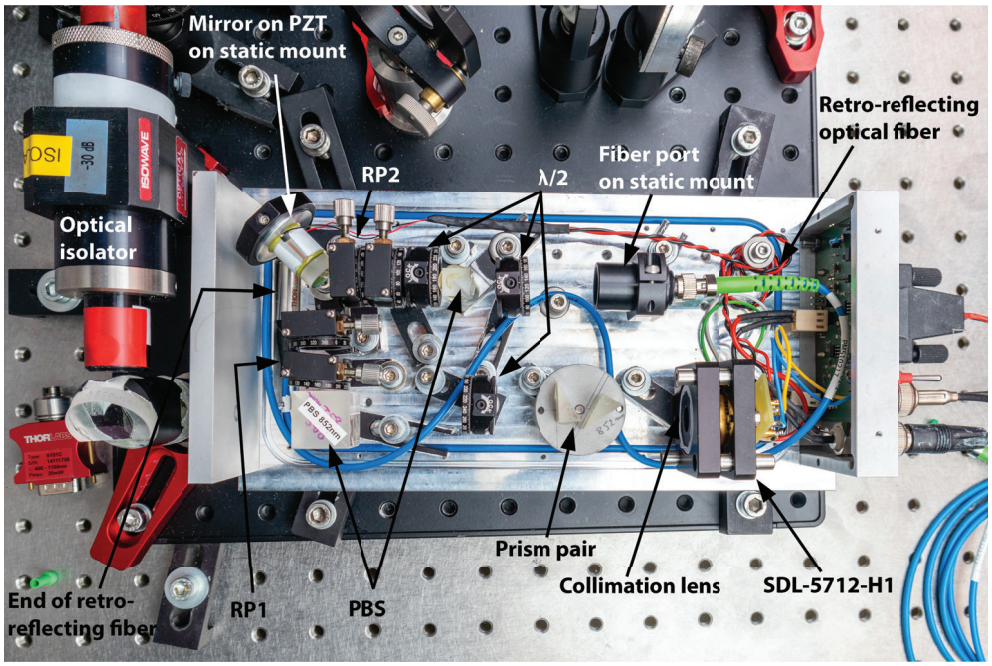

Figure 24: Photo of the ECDL setup with two Risley prism pairs (RP1 and RP2) in the custom-built aluminium housing. The static mounts for the mirror on the PZT and the fiber port can also be seen.

3.1.3 Procedure of Coupling Light into a Retro-Reflecting Optical Fiber

To measure the portion of light that effectively couples into the optical fiber, a ThorLabs P3-780PM-FC-2 polarisation maintaining optical fiber [9] is used in the first ECDL setup as well as in the second setup. With this, the end of the optical fiber can be attached to a power meter sensor, thus it is easy to measure how much light is coupled into the fiber. Since the coupling of an optical fiber is very sensitive, removing the standard fiber and attaching the retroreflecting fiber means that the fiber port is shifted slightly and the coupling is worse. The procedure to couple the light into the retro-reflecting optical fiber is the following: First, the setup is roughly aligned with the standard optical fiber by sending light from a laser pointer from the end of the fiber back along the ECDL path. By overlapping the incoming light from the diode with the light from the laser pointer in front of the fiber port and in front of the mirror on the PZT, the rough alignment is done. Next, the end of the standard fiber is attached to a power meter sensor, performing a standard beam-walking technique to maximise the power detected with the power meter. After that, the standard fiber is carefully removed and swapped out with the retro-reflecting fiber. Then, a $\lambda/4$ is placed in front of the fiber mount. With this, the polarisation of the back-reflected light is tilted and the back-reflected beam exits the PBS to the side of the setup, where a power meter is placed to monitor the power of the back-reflected light. By moving the stages of the PZT and the fiber port (adjusting the Risley prism pairs), the power of the back-reflected light is maximised to achieve a maximum of around 50% of coupling to the optical fiber. Another way to demonstrate that the optical feedback is doing it's job, is to send the outgoing beam to a Fabry-Perot interferometer (FPI) and display it's signal on an oscilloscope. One can see by eye the resonant peaks in the FPI getting narrower and also high-frequency noise from the bare DBR diode getting reduced when the coupling to the fiber is sufficient to feed back light into the diode.

3.1.4 MTS setup

The rest of the experimental setup is the same for both cases (orange rectangle in figure 23): The outgoing beam exiting the ECDL setup traverses an optical isolator, to avoid any unwanted back-reflections being fed-back into the DBR diode. Then a $\lambda/2$ and a PBS (PBS3) are used to again split the beam: one is used as the output beam (high power) and the other one is used to feed the MTS setup. Here, the beam splits up into the probe beam (red arrows) and the pump beam (black arrows) using a $\lambda/2$ and a PBS (PBS4). The probe beam directly enters the Cs vapour cell, whereas the pump beam travels through an EOM and enters the Cs vapour cell in opposite direction to the probe beam. The so produced MTS signal is sent to a photodiode (PD) via another PBS (PBS5), where the lens L1 is used to focus the probe beam onto the PD. A photo of this setup is shown in figure 25.

3.2 Electronic Setup

The electronic setup to control and stabilise the laser frequency actively can be seen in figure 26. It is to note that the electronic setup is the same for both ECDL setups used. A home-built EOM controller (EOM box) produces a modulation frequency Ω, which is fed to the EOM itself to modulate the pump beam. The MTS signal is detected by a photodiode (PD) and sent back to the EOM box, where the error signal is produced. This error signal is then fed into a home-built proportional-, integral- and derivative-servo (PID). The PID controller has a slow and a fast output. The slow PID output is fed into a home-built PIEZO controller, where the signal from the PID is added as a modulation onto a DC signal, which controls the PZT and therefore the cavity length in the ECDL setup. The fast PID output is used to directly modulate the DBR diode's current. In addition, all signals from the PID controller can be displayed on an oscilloscope.

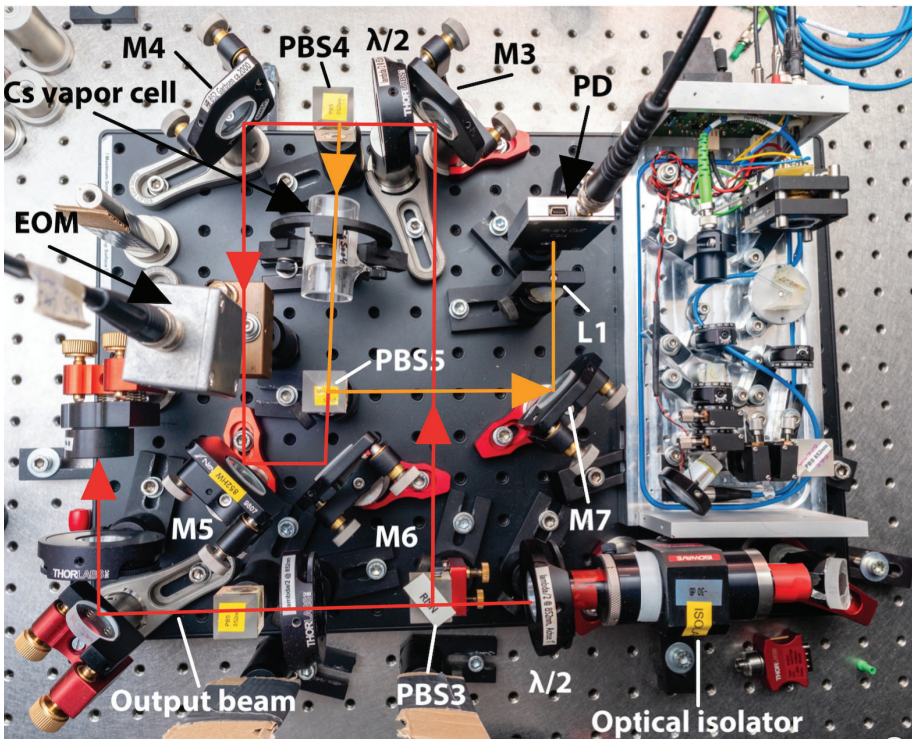

Figure 25: Photo of the full setup with the ECDL setup on the right. Beam paths are indicated with the red lines/arrows. In the MTS setup, the orange beam path indicates the probe beam, where the counter-propagating red beam shows the pump-beam. The output beam path to another fiber coupling stage is also shown on the bottom left of the photo.

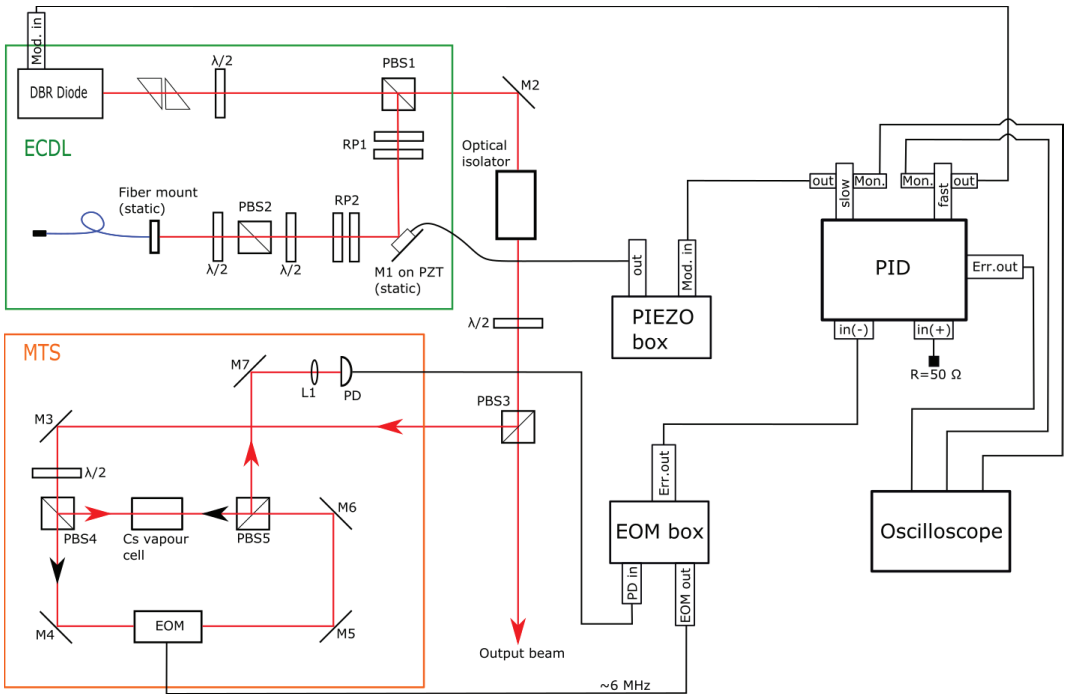

Figure 26: Electronic setup in addition to the optical setup from figure 23: PID - proportional-, integral- and derivative servo; Err. out - error signal output; Mon. - monitor output; PIEZO box - piezo control box; Mod. in - Modulation input; EOM box - EOM control box; PD in - photodiode input; EOM out - EOM output for modulation.

4 Characterisation of the Setup

In this chapter, the experiment will be described and characterised. First, the bare DBR diode is tested and the threshold current is determined. After knowing the basics of our laser, we dive into the first setup for the ECDL laser system which was introduced in section 3.1.1. After that, the focus shifts to the second ECDL setup introduced in section 3.1.2.

4.1 Threshold Current of the DBR Laser Diode

Before jumping into the more complex elements of this experiment, the threshold current of our DBR laser diode SDL-5712-H1 is measured according to section 2.4.1. The laser output power is measured against the current driving the laser diode. A profile LDC200 laser diode controller is used in combination with a Tektronix TED 200 temperature controller to drive the laser diode. The data points are plotted in figure 27, where also a linear regression is shown in red. This linear function is described by $P = a \cdot I + b$, where P is the output power, I the diode current, a the slope and b the offset. Here, 14 data points between 30 mA and 100 mA were used to determine the fit parameters

$$a = 0,711(5) \text{ and } b = -16,6(3). \tag{70}$$

The errors for a and b result from performing a linear fit to the data points in QtiPlot. Calculating where this linear regression intersects with the horizontal axis gives a threshold current of

$$I_{\text{th}} = 23,3(4) \text{ mA}. \tag{71}$$

Here, the error for the threshold current is calculated from error propagation. We can also see that this DBR laser diode SDL-5712-H1 can give up to about 90 mW of output power, which will be sufficient for our experiment. Unfortunately, we could not find a datasheet or an operation manual for our laser diode. However, a table was found in [42], which is shown in figure 28. The threshold current from our measurement does not fit the value of $I_{\text{th}} = 29$ mA given in figure 28 and also the slope efficiency, which basically is our fit-parameter a, is a bit off to our measurement. I_{max} was set on our laser diode current controller to a maximum value of 160 mA just to be safe since we got plenty of power out of the laser diode already at lower currents. For the optical feedback in the ECDL setup, some 100 μW are enough and in the MTS setup, less than 10 mW of optical power is needed. Thus, this laser system should be able to give a net output power of useful laser light of up to about 80 mW.

4.2 ECDL Setup with Movable Mirror Mounts

We first want to concentrate on the setup shown in figure 21. Here, the ECDL setup is built with classical movable mirror mounts for the mirror on the Piezo transducer (PZT) and the fiber port, which can be seen more clearly in figure 22. The first task was to align the laser diode, the collimation lens and the following prism pair to create a circular beam shape. This is important because the more circular the beam gets, the more of it we are able to couple into the optical fiber. The laser diode itself is sitting in a TO-3 laser diode mount [6], where the position of the laser diode can be adjusted with two screws. When the laser diode is sitting in the right place, the laser light travels right through the middle of the collimation lens. This lens is then adjusted by bringing it closer or further away from the laser diode. The correct distance between the diode and the collimation lens is achieved when the laser beam is collimated over large distances (in our case, the beam was displayed on a screen on the opposite wall of the lab about 5 m away). The prism pair is then used to shape the elliptical beam into a circular beam by slightly rotating it. The beam shape was then measured with a Thorlabs BC 106-VIS beam profiler to be $x = 2290(20)$ μm and

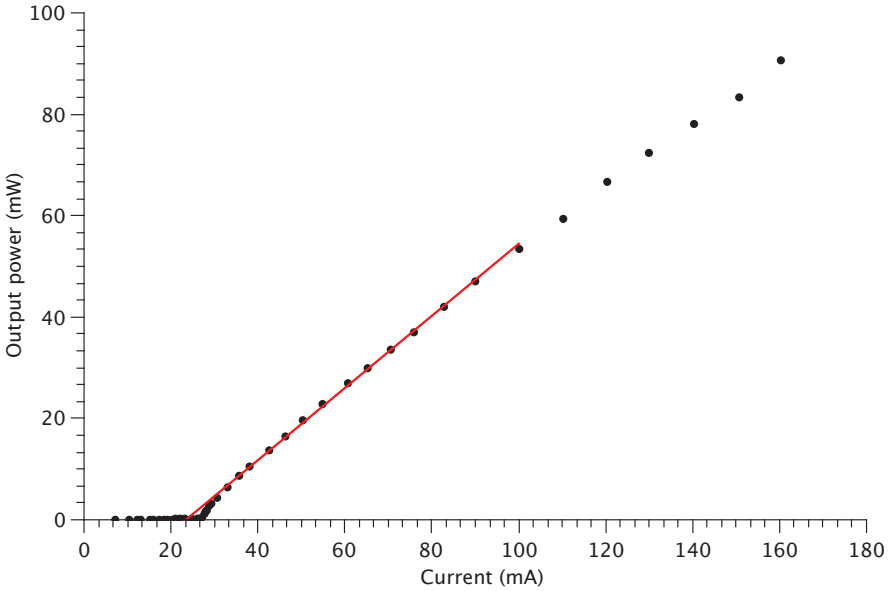

Figure 27: Output power versus diode current for the DBR laser diode SDL-5712-H1. A linear regression $P = a \cdot I + b$ is shown in red, where 15 data points between 30 and 100 mA were used. The output power was measured with a Thorlabs PM100D power meter with a Thorlabs S120C power head. The uncertainty from the power meter is given by ± 3% [4]. The diode current was directly read off the LDC200 laser diode controller by profile (which is now taken over by Thorlabs) and has a uncertainty in constant current output of ±20 μA [13]. Because the errors on the vertical and the horizontal axis are that small, they are not shown in the plot.

$y = 2230(10)$ μm. With this, we can already calculate the focal length of the lens we need to couple the laser light into the optical fiber. Both our test-fiber P3-780PM-FC-2 and the retroreflector fiber P5-780PMR-P01-1 have a numerical aperture of $0,12$. With the help of equation (58), the desired focal length for our lens is about 9mm. Since this exact focal length is not available, we are using the next closest focal length, which is a C220TM-B $f = 11$ mm aspheric lens by Thorlabs [3]. With all the components for the ECDL setup mounted to the optical table, we first attach our test-fiber to measure the power coupled to the optical fiber with a Thorlabs PM100D power meter and a Thorlabs S151C fiber power sensor. The idea is to maximise the coupling to the test-fiber first to get an idea of how much light can be coupled into the fiber, which was around 50% and maxed out at 60% eventually. Then the test-fiber is removed and the retroreflecing fiber attached. To measure and quantify the coupling to the retroreflecing fiber, we used a $\lambda/4$ waveplate in front of the fiber coupler, so that the polarisation of the reflected light coming out of the fiber is tilted. This makes it possible to separate the back-reflected beam from the incoming laser beam at the PBS2 and the power of the back-reflected light can then be measured to the side of the setup at the PBS2 with a power meter. Of course, the swap from one fiber to the other destroys the coupling achieved before. But since only the mount where the fiber is attached is touched when swapping the fibers, it is a relatively easy and fast procedure to achieve about the same coupling to the retroreflector fiber by maximising the power measured at the PBS2 only adjusting the two screws on the fiber mount.

4.2.1 First Results of Laser Narrowing

After aligning the ECDL setup, the MTS setup (orange rectangle in figure 23) is aligned to generate an error signal. In order to get a signal out of the MTS setup, a 50 Hz triangle function from a function generator is applied directly to the laser current via a modulation input on the Profile

Data for SDL-5712-H1 DBR Laser Diode		
Tuning [a]		
Temperature	0.07	nm/deg
Current	0.003	nm/mA
	1.24[b]	GHz/mA
Mode hop seperation	0.08	nm
	27	mA
Efficiency and Electronic Characteristics [c]		
Differential Q.E.	0.47	
Slope Efficiency	0.68	mW/mA
I_{th}	29	mA
I_{max}	179	mA
P_{max}	100	mW
R	3.21	ohms
Beam Characteristics [d]		
Beam Divergence θ_{FWHM}		
$\perp$ to facet	30	deg
$\parallel$ to facet	10	deg
Bandwidth	3	MHz

[a] SDL Operators Manual
[b] conversion @ 852 nm
[c] Laser Data Sheet
[d] SDL Catalog

Figure 28: Some data to our DBR laser diode SDL-5712-H1. Unfortunately we did not have any datasheet or operation manual for our laser diode. This table was the only thing we could find online. Table found in [42].

Laserdiode Controller LDC200. The oscilloscope data plotted in figures 29 (a), (b) and (c) show the first evidence that the optical feedback is working. The time axis on the oscilloscope is converted into a frequency axis by measuring the time difference between two atomic lines in figure 29 (a), where we know the frequency between them is 251.00(2) MHz [50]. That said, the first peak of the absorption spectrum where the error signal has it's zero-crossing is the $6^2\mathbf{P}_{3/2}$, F= 5 and the next peak the $6^2\mathbf{P}_{3/2}$, F= 4 hyperfine line. In figure 29 (a) no optical feedback is applied and some high-frequency noise overlapping with the error signal is observed. The error signal has a slope of $15,8(7)\ \frac{\text{mV}}{\text{MHz}}$. In figure 29 (b) the optical feedback power is set to about 35 μW. A reduction of high-frequency noise in the error signal can be seen, although it is still present. The error signal slope steepens to $17,3(7)\ \frac{\text{mV}}{\text{MHz}}$. In figure 29 (c) the optical feedback power is increased to about 100 μW which further decreases the noise but flattens the slope of the error signal to $6,21(3)\ \frac{\text{mV}}{\text{MHz}}$. The absorption signal is showing some strange plateaus. We think that the optical feedback is forcing the laser to stay in the same mode until a mode-hop to another plateau occurs. This is also a sign that the optical feedback is working properly. If we compare figure (a) to figure (c), the error signal slope has more than doubled in height from about 400 mV peak-to-peak to about 890 mV peak-to-peak. The frequency interval over which the error signal evolves on the other hand has gotten bigger in figure (c) to about 150 kHz, as it was about 60 kHz in figure (a). We think that this behaviour is also a result from the optical feedback broadening the individual absorption lines by holding the laser on the external cavity's resonance, before a mode-hop to the next resonance occurs. Although no conclusions can be drawn from these pictures, because of the scanning on the laser diode current, it shows that the optical feedback is working and it can be seen that the high-frequency noise on top of the error signal is reduced.

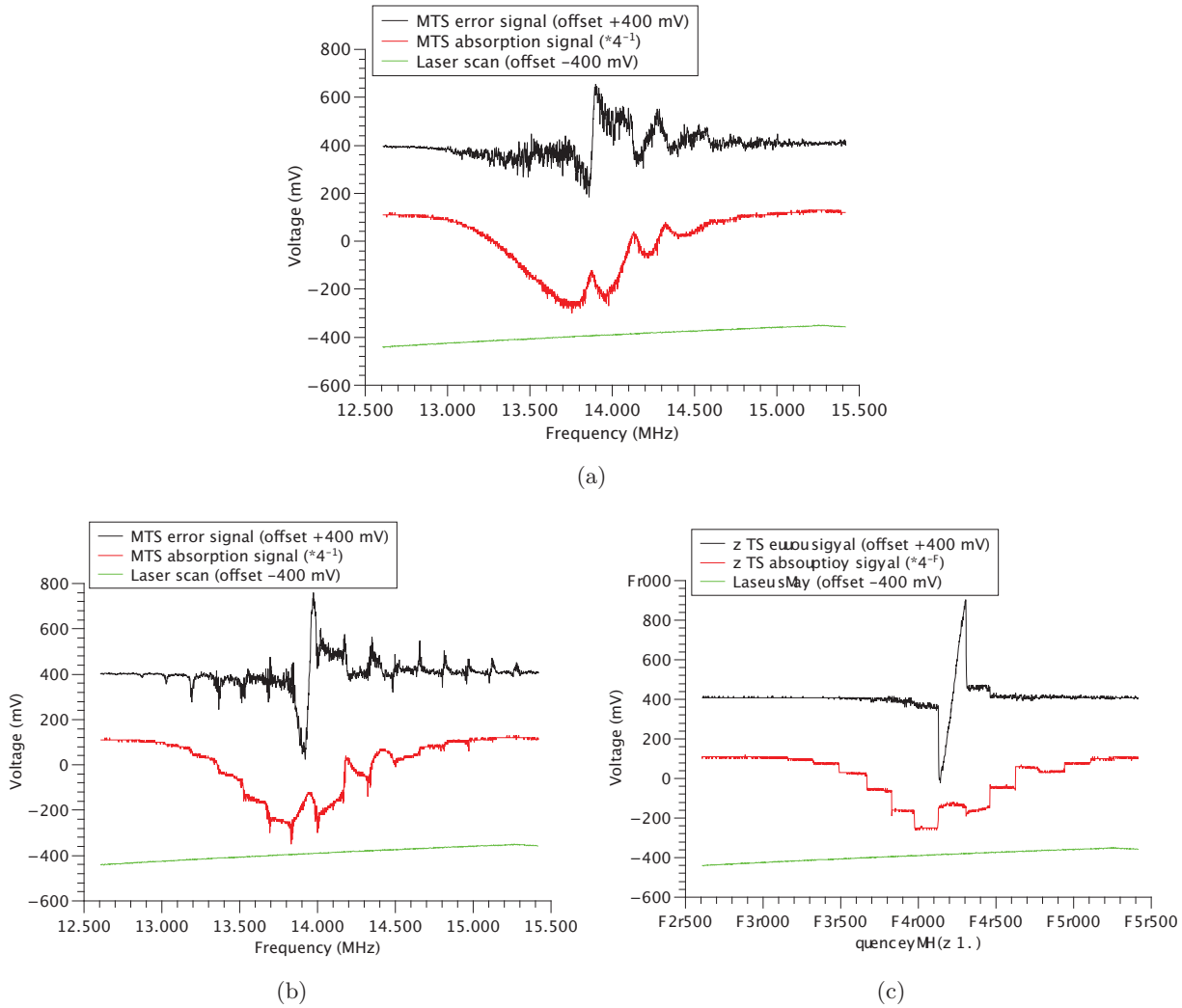

Figure 29: MTS error signal in black, MTS absorption signal (Doppler-free) in red and the laser scan in green. (a): no optical feedback was introduced. (b): optical feedback power of about 35 μW. (c) optical feedback power of about 100 μW.

4.2.2 Using the Pound-Drever-Hall Technique to generate an Error Signal

After testing the MTS setup and getting an error signal out of it, we wanted to test our laser in a commercial Fabry-Perot Interferometer (Toptica FPI 100-01106, Series DL-100, 750 nm, 1 GHz), since it is easier to see the laser lines. Another advantage is that we could test our PID servo by locking the laser to the FPI. To get an error signal, we opted for the widely used Pound-Drever-Hall technique. This thesis will not go into detail of this technique, so the interested reader may find Eric Black's introduction to the PDH technique useful [44]. The setup to create a PDH error signal is shown in figure 30. The output beam shown in figure 23 is coupled into a fibered EOM where the beam is modulated to create sidebands. This modulated beam is then sent to the FPI. To monitor the transmission spectrum of the FPI, the built-in photodiode at the back end of the FPI is used, which has an amplifier in the Toptica miniScan 102 scan generator for this specific FPI (not shown in figure 30). This said scan generator is of course also used to scan the piezo-transducer sitting on one end of the FPI to scan the cavity. To get the PDH error signal, the reflected light from the FPI is used. The reflected light from the FPI was separated from the incoming light beam

with a $\lambda/4$ waveplate in combination with a PBS to send the reflected portion of light from the FPI through a focusing lens to a homebuilt photodiode. Figure 31 (a) and (b) show some data obtained with this setup. In figure 31 (a) no optical feedback was given to the laser diode. The transmission signal is so noisy that the two weak sidebands can only barely be seen. Also the PDH error signal has some clearly visible high-frequency fluctuations to it. The slope of the error signal measures 233(31) $\frac{\text{mV}}{\text{MHz}}$. If we compare these signals to the ones in figure 31 (b), a reduction in high-frequency noise is observed when optical feedback is added to the laser system. In this case, the optical feedback power is about 430 μW and the slope of the PDH error signal is measured to be 171(38) $\frac{\text{mV}}{\text{MHz}}$, which is a huge improvement compared to the slope of the PDH error signal in figure (a). Since we now know that the optical feedback in our ECDL system is working, the next step is to measure the linewidth of our laser. For this, we continued using the FPI to measure the noise spectral density.

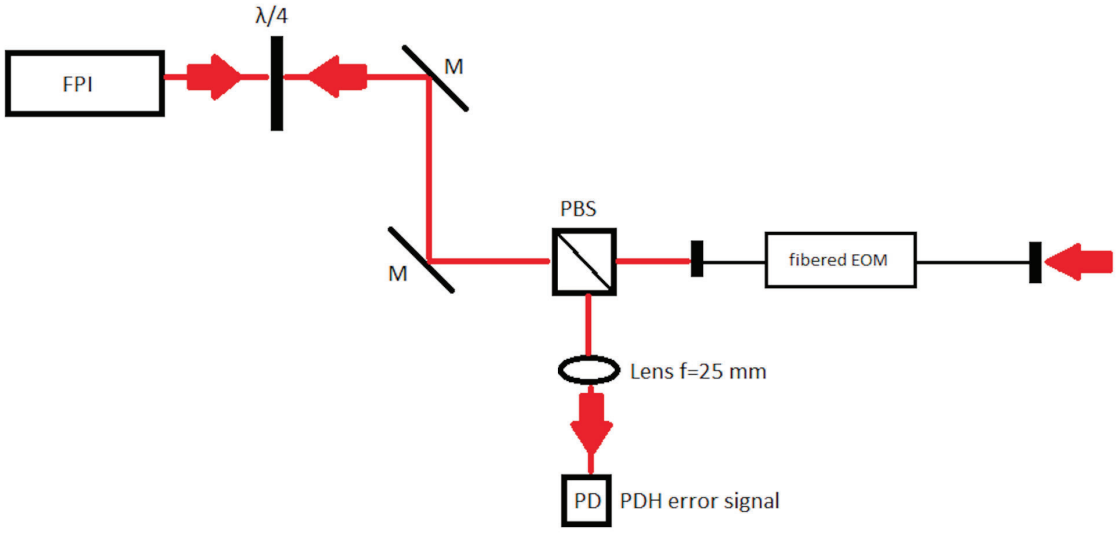

Figure 30: Setup to create a PDH error signal using a commercial FPI.

4.2.3 Noise Spectral Density

To determine the linewidth of our laser, we measure the noise spectral density of the error signal. This is done by holding the laser on the FPI's resonance by a weak lock and sending the error signal to a spectrum analyser. The linewidth is then calculated from this data using equation (39). To measure the NSD of the free-running laser system with optical feedback applied, the laser needs to stay on the FPI's resonance for several seconds in order to have enough time to take a meaningful measurement with a Stanford Research Systems SR1+ Audio Analyser [2]. Unfortunately, the laser jumped off the FPI's resonance so quickly and uncontrolled, that we could not perform a measurement. To hold the laser on the FPI resonance for the time of the measurement, the laser is slightly locked to the FPI. This very weak locking is performed using the fast P- and I- part of the PID servo ($<$ 14 kHz locking bandwidth, which is well below the resolution bandwidth of the audio analyser), but with the minimum possible gain to not control the laser too much, since we are interested in the NSD of the laser system without any locking scheme applied. Figure 32 compares the PDH error signal and the FPI transmission signal when (a) no locking scheme is applied (same plot as in figure 31 (b)) to (b) when the fast P-part and (c) the fast P- and I-part of the PID servo is turned on with a minimum possible gain. The error signal slope in figure 32 (b) compared to (a) flattens slightly, signalling that the polarity of the PID servo is chosen correctly. Since only

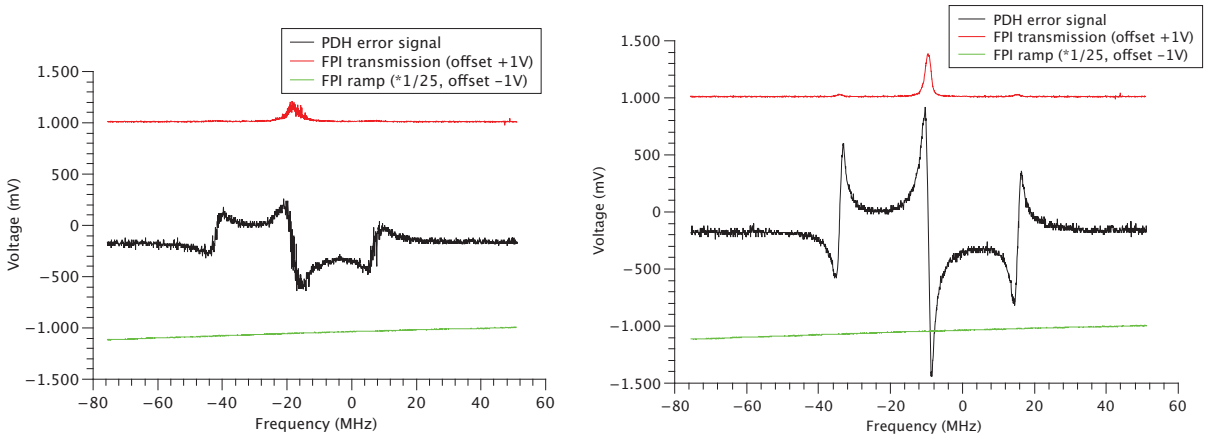

Figure 31: FPI transmission signal in red, PDH error signal in black and FPI scan signal in green. (a): No optical feedback. The error signal slope is $\frac{5{,}02\ \text{MHz}}{0{,}84\ \text{V}}$ (b): Optical feedback power $\approx 430\ \mu$W. The error signal slope is $\frac{1{,}62\ \text{MHz}}{2{,}36\ \text{V}}$.

using the fast P-part was not enough to hold the laser on the FPI's resonance long enough, the fast I-part is turned on additionally, flattening the error signal slope even more in figure 32 (c). In figure 33 the noise power spectrum of the PDH error signal is shown, where the DBR diode was given 435(3) μW of optical feedback power and the fast P- and I-part of the PID servo were used with minimal gain. The data was saved in units of $\frac{\text{V}}{\sqrt{\text{Hz}}}$ and transformed to units of $\frac{\text{Hz}}{\sqrt{\text{Hz}}}$ by using the error signal slope that was measured at the same value for the optical feedback power. Within the first 1 kHz we see some resonances at about 230, 360 and 550 Hz which we assume to come from mechanical resonances in the springs of the moveable mirror- and fiber-mount in the ECDL setup. When we look at frequencies above 1 kHz, some constant white noise can be seen which is expected to remain constant for even higher frequencies where our audio analyser cannot measure anymore. Using equation (39) and an upper integration limit of 8 kHz, the linewidth is determined to be

$$\Delta\nu_1 = 72(3)\ \text{kHz}. \tag{72}$$

The error arises from the PDH error signal, where error propagation is used to determine the error for each value of the NSD. The upper integration limit of 8 kHz is chosen because above 8 kHz, only white noise characteristics is observed. We see in the data plotted in figure 33, that the biggest contribution to the obtained laser linewidth comes from the peaks within the first 1 kHz. This can also be seen in figure 34 (a), where the FPI scan is turned off and the laser is tuned manually to the FPI's resonance to display the FPI transmission signal fluctuating, with the same optical feedback power applied. A Fourier Transform of this data in figure 34 (b) shows a similar spectrum to the one in figure 33, where the big contribution to the overall spectrum from the peaks within the first 1000 Hz is displayed again. The goal then became clear: we have to suppress these resonances to bring down the linewidth even further.

The noise spectral density of the error signal is also measured without optical feedback applied. This measurement is of interest, because since we do not have a datasheet for our laser diode, we want to have some number for the linewidth of the bare DBR diode. To hold the laser on the FPI's resonance, the fast I-part of the PID servo has to be used to talk directly to the laser current and hold the laser on the FPI's resonance for the time of the measurement (locking bandwidth again < 14 kHz). Knowing that this already can narrow the diode's linewidth, again the fast I-part is

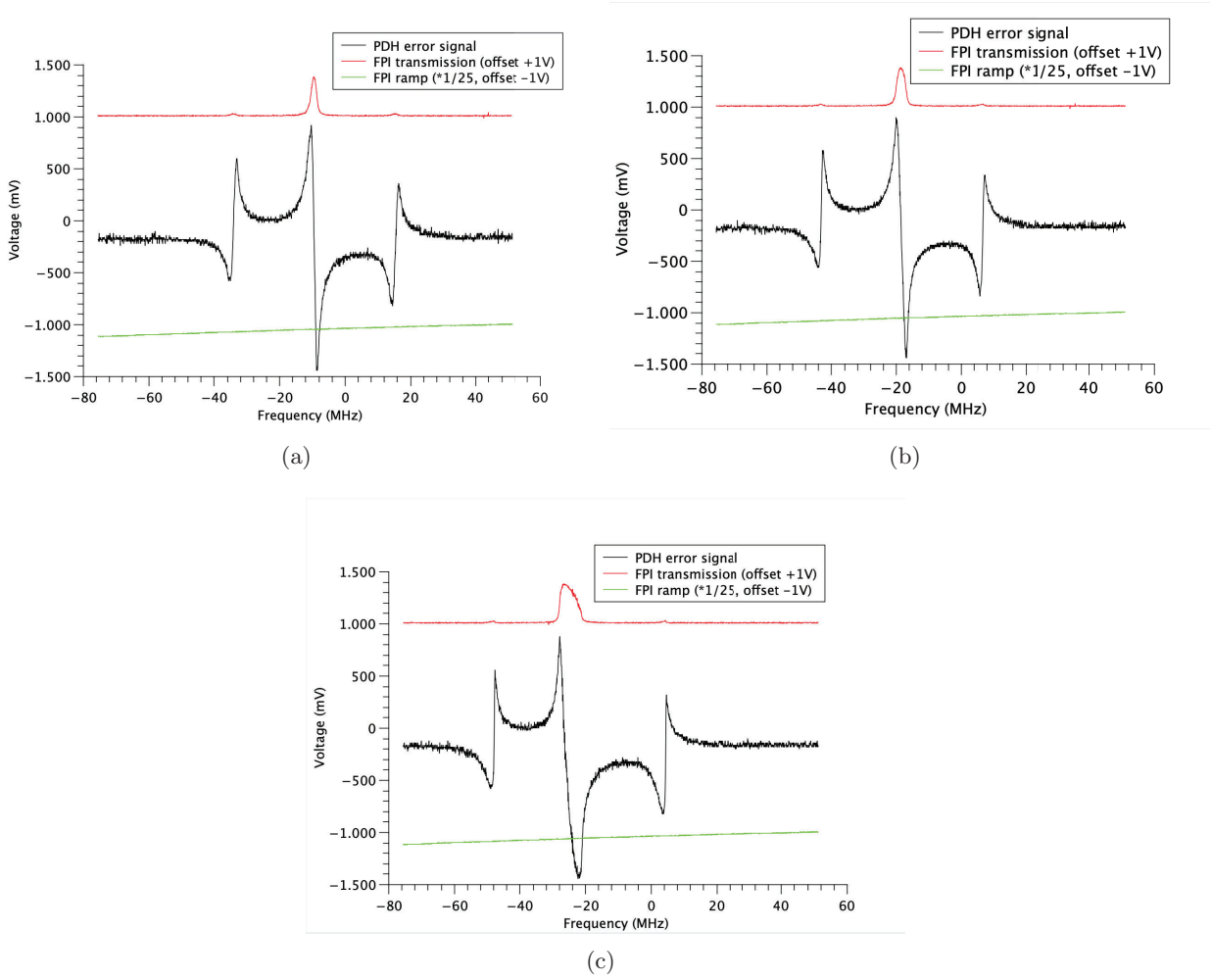

Figure 32: PDH error signals and FPI transmission signals: (a) Same data as in figure 31 (b) for comparison, no locking scheme applied. (b) Turning on the fast P-part of the PID servo results in a slight flattening of the error signal slope, signalling the polarity of the servo is correct. (c) Turning on the fast P- and I- part of the PID servo lets the error signal slope flatten even more, again signalling that the polarity of the locking scheme is correct.

used with a minimal possible gain to not control the laser's current too much. In figure 35, the noise spectral density up to 29 kHz is shown on a double logarithmic scale. Again using equation (39) yields a linewidth of

$$\Delta\nu_{\text{DBR, high RES}} = 2,57(1)\ \text{MHz}, \tag{73}$$

where the integration is performed over the whole spectrum. Another measurement with the bare DBR diode without optical feedback is performed in figure 36, but this time with the audio analyser set to high bandwidth mode to display the spectrum above 29kHz. Again for this data we can calculate the linewidth and get

$$\Delta\nu_{\text{DBR, high BW}} = 4,13(2)\ \text{MHz}, \tag{74}$$

where again the integration is done over the whole spectrum. When the integration is only performed up to 29 kHz like in the case of the high resolution measurement, the linewidth is $4,08(2)$ MHz. These two very different results show, that although helping the laser via the fast I-part of the PID servo to stay on the cavity's resonance, it is very unstable there and these two results can only

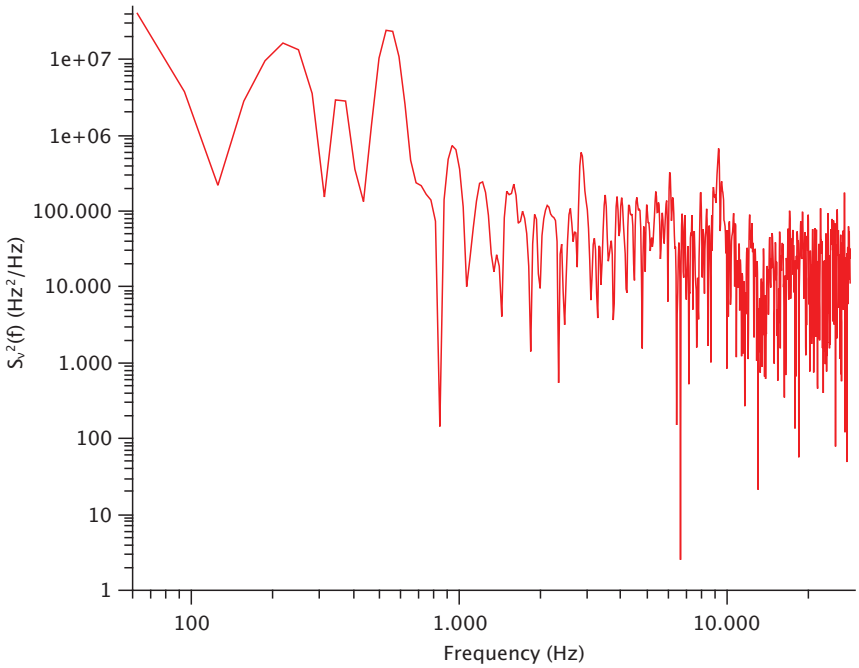

Figure 33: Noise spectral density at an optical feedback power of 435(3) μW. One can clearly see some peaks within the first 1 kHz of the data. These peaks give the biggest contribution to the calculation of the linewidth. Above around 1 kHz, white noise characteristics are observed.

guide us to where the linewidth of the bare DBR diode lies. Given that we talked to the current of the laser diode via the PID, it is assumed that the linewidth of the bare DBR diode is even higher than $\Delta\nu_{\text{DBR, high BW}}$, on the order of $\sim$ 10 MHz. As a result, the linewidth could be reduced by three orders of magnitude by implementing optical feedback.

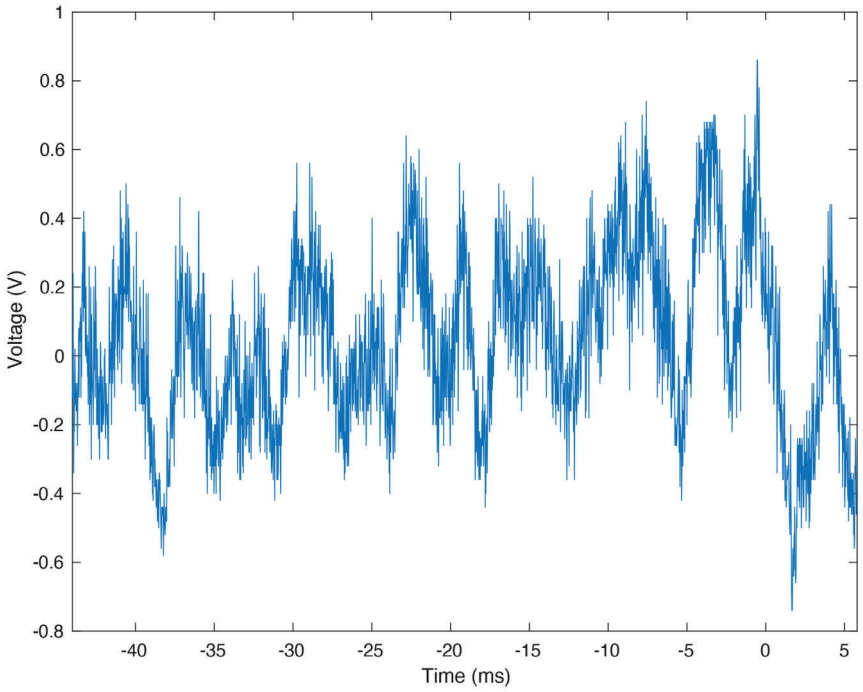

(a)

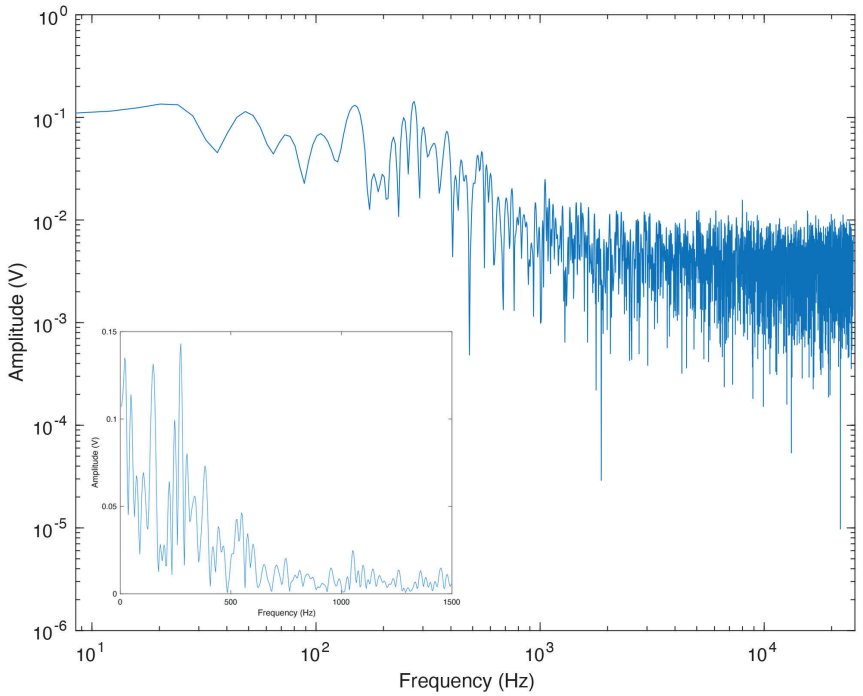

(b)

Figure 34: (a) FPI transmission signal without FPI scan applied. The laser was tuned manually onto the FPI's resonance. The optical feedback power was held constant at 435(3) μW. (b) Fourier Transformation of the data in (a) shows a very similar spectrum to that in figure 33. The plot is on a double logarithmic scale. The insert shows the same data on a linear scale.

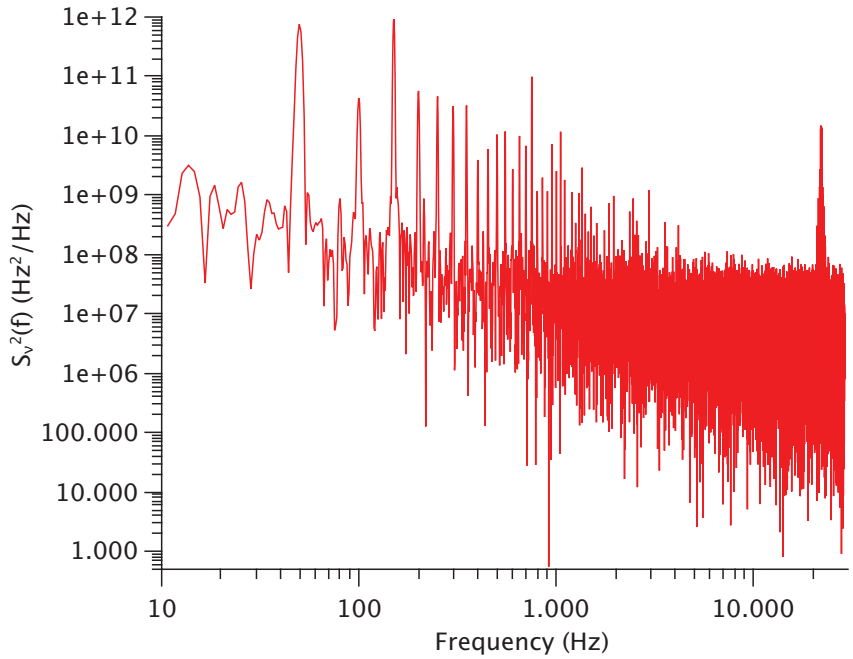

Figure 35: Noise spectral density of the DBR diode without optical feedback applied. The audio analyser was set to high resolution mode with 32k measurement points. The fast I-part of the PID servo was used with a minimal possible gain to hold the laser on the FPI's resonance for the time of the measurement.

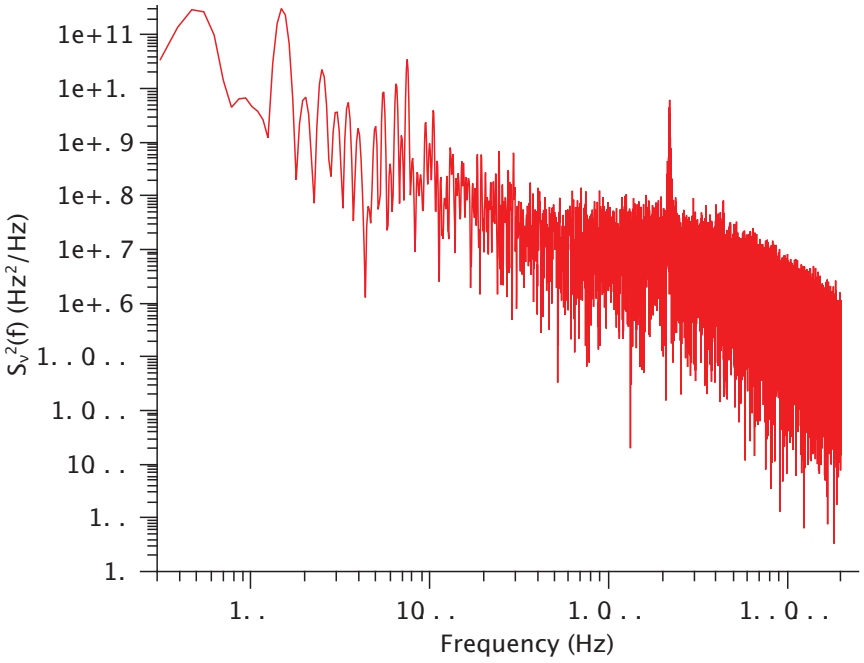

Figure 36: Noise spectral density of the DBR diode without optical feedback applied. The audio analyser was set to high bandwidth mode to see the spectrum above 29 kHz, which cannot be seen in figure 35. The fast I-part of the PID servo was used with a minimal possible gain to hold the laser on the FPI's resonance for the time of the measurement.

4.3 ECDL Setup with two Risley Prism Pairs

For the second ECDL setup, the idea is to make the laser system less acceptable to acoustic noise, which is showing up in figure 33 within the first 1 kHz. To accomplish this, we essentially did two things: First, we designed an aluminium housing, which was custom-built and includes the whole ECDL setup built with half-inch optics instead of one-inch optics to trim down the size of it. The second change is to eliminate all moveable parts in the ECDL setup. We have done this by getting rid of the moveable mounts for the mirror on the PZT and the fiber port. These components are now bolted to the custom baseplate and are fixed. Since these moveable mounts were originally used to move the beam and to align the coupling to the optical fiber, some other mechanism is needed to be able to steer the beam precisely into the optical fiber. For this, we are using two Risley prism pairs built with Edmund Optics 2° wedge prisms for visible - near infrared (VIS-NIR) wavelengths with a $12,5$ mm diameter (half-inch) [1] mounted in Thorlabs PRM05/M high-precision rotation mounts [11]. The rotation of these mounts can also be fixed by tightening a small bolt on the mount after alignment. As can be seen in figure 24, a channel for the retro-reflecting optical fiber is machined into the baseplate, to keep the fiber as steady as possible. Another change compared to the previous setup had to be done: taking the laser diode out of the original housing (black housing on the bottom right in figure 22) and soldering some new wires to the TO-3 laser diode mount. By doing this, we changed the electronic control board of the laser diode so that all wires exiting the ECDL setup do so on the back of the aluminium housing. We then directly bolt the mount [6] containing laser diode and collimation lens to the new baseplate.

After building up this setup, the diode, the collimation lens and the prism pair is aligned again and the beam shape is measured with a Thorlabs BC-106VIS beam profiler at the fiber port to be $x = 2942(10)$ μm and $y = 2725(10)$ μm.

Then we again send the light to a Fabry-Perot cavity to produce a PDH error signal like it is discussed in section 4.2.2. In figure 37, the noise spectral density of the PDH error signal is shown as a high resolution measurement with 32k measurement points. Optical feedback power of 420(10) μW is implemented. Again the PID servo needs to be used to hold the laser on the FPI's resonance. Only using the slow P- and I- part of the servo to talk to the PZT in the ECDL path to control the external cavity length showed oscillation of the error signal despite turning the gain knobs to the minimum. By adding the fast P- and I-part of the PID servo to additionally control the laser diode's current, these oscillations could be suppressed. The locking bandwidths are 34 Hz for the slow PID part and < 14 kHz for the fast PID part, both well below the resolution bandwidth of the audio analyser. This measurement now shows the laser locked to the FP cavity, although the locking scheme was very weak since the FPI's resonance could not be held for longer than about 30s. This of course is also intensified by the FP cavity not being stabilised in temperature and mechanically. An integration over the whole spectrum using equation (39) gives a linewidth of

$$\Delta\nu_{2,\text{ high RES}} = 5,7(2)\text{ kHz}. \tag{75}$$

A second measurement with the audio analyzer set to high bandwidth mode is shown in figure 38. The PID servo and optical feedback power were held constant. Integration over the whole spectrum yields a linewidth of

$$\Delta\nu_{2,\text{ high BW}} = 7,526(3)\text{ kHz}, \tag{76}$$

whereas an integration up to 29 kHz gives

$$\Delta\nu_{2,\text{ high BW, 29kHz}} = 5,576(2)\text{ kHz}, \tag{77}$$

which lies within the error of $\Delta\nu_{2,\text{ high RES}}$.

Measuring the laser in this configuration with the aluminium housing closed and with the lid opened did not show any significant difference. Compared to the first ECDL setup, where moveable

mirror mounts were used, the linewidth of the laser could be reduced from 72(3) kHz to 5,7(2) kHz. We assume a big part of this improvement is due to the moveable parts in the setup being eliminated. Compared to the bare DBR diode, lasing with a linewidth on the order of 10 MHz, the linewidth could be reduced by four orders of magnitude.

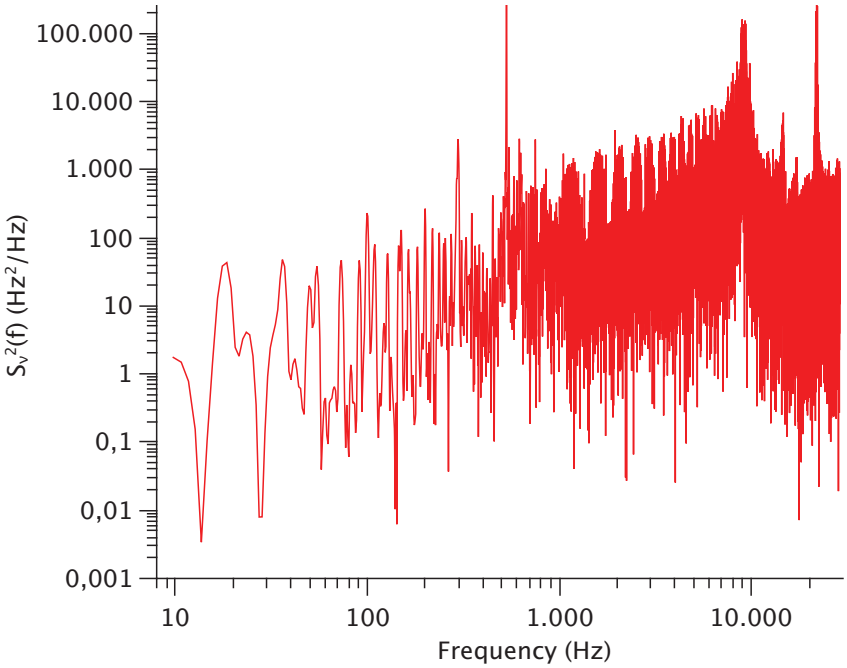

Figure 37: Noise spectral density of the DBR diode with 420 μW of optical feedback power applied. The audio analyser was set to high resolution mode with 32k measurement points. To hold the laser on the FPI's resonance, the slow P- and I-part and the fast P- and I-part of the PID servo were used with a minimal possible gain.

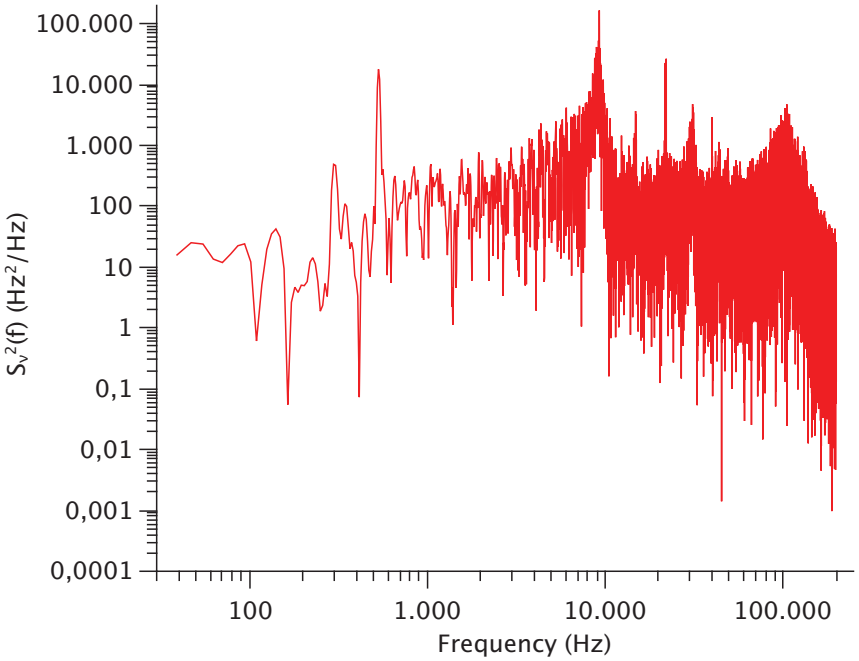

Figure 38: Noise spectral density of the DBR diode with 420 μW of optical feedback power applied. The audio analyser was set to high bandwidth mode to show the spectrum above 29 kHz. To hold the laser on the FPI's resonance, the slow P- and I-part and the fast P- and I-part of the PID servo were used with a minimal possible gain.

5 Summary

The goal of this thesis is to build an ECDL laser system with the use of a retro-reflecting optical fiber to extend the external cavity. A DBR laser diode at 852 nm is used in combination with a MTS setup on Cesium vapour at room temperature to obtain an error signal and to electronically control the laser. The Cesium transition of interest is the D2 transition from $6^2S_{1/2}$ $F = 4$ to $6^2P_{3/2}$ $F = 5$ with a frequency splitting of $2\pi \cdot 351{,}721\ 933\ 533\ (111)$ THz.

Section 2 discusses the basic principles of what is important to understand this thesis and also introduces a beam steering technique using prisms, that is used in sections 3.1.2 and 4.3.

In section 3, the experimental setup is described. In the first iteration of the experiment (section 3.1.1), movable mirror mounts are used to couple the light in the external cavity into the retro-reflecting optical fiber. The following section 3.1.2 already introduces the second setup of the experiment, where the movable and spring-loaded mounts in the ECDL path are replaced by two Risley prism pairs, that are discussed in section 2.11.

The procedure of coupling light into a retro-reflecting optical fiber is discussed in section 3.1.3. A standard optical fiber is used in combination with an additional laser pointer to align the setup roughly. After maximising the power of light coupled to the standard fiber, which is measured with a power meter connected to the end of the fiber, the retro-reflecting optical fiber is attached. The polarisation of the back-reflected light from the retro-reflecting fiber is tilted by an additional $\lambda/4$ waveplate placed in front of the fiber port, to measure the power with a power meter to the side of the setup after a PBS.

Section 3.2 goes through the electronic setup of the experiment, where a large part consists of home-built electronics. A commercial diode current controller and diode temperature controller are used to operate the laser diode. The photodiode, PID servo, EOM modulation box and the high-voltage amplifier for controlling the PZT are all home-built.

The results are presented in section 4. First, the DBR laser diode itself is tested in section 4.1, where a threshold current of $23,3(4)$ mA is found. It is also shown, that the laser diode has a power output of up to about 60 to 80 mW, depending on the current it is run on, which is more than sufficient for our use.

In section 4.2, the first ECDL setup with spring-loaded and movable mirror mounts for the fiber port and the PZT is built up and characterised. We present the first results of decreasing the high-frequency noise in the laser in section 4.2.1. The MTS setup is used to produce an error signal that shows a decrease in high-frequency noise for the laser operated with about 10 μW of optical feedback power and even a higher decrease for the laser operated with about 100 μW of optical feedback power, compared to the bare DBR diode without optical feedback.

In the following sections 4.2.2 and 4.2.3, the Pound-Drever-Hall technique is used to generate an error signal using a commercial FPI. The decrease in high-frequency noise can also be seen on the PDH error signals and the FPI transmission signals. The PDH error signal is then used to measure the noise spectral density of the signal using a spectrum analyser. The fast P- and I-part of the PID servo were used to hold the laser on the FPI's resonance for the time of the measurement with very weak gain applied. This data is shown in figure 33 and yields a laser linewidth of 72(3) kHz without any locking scheme applied. The strong resonant peaks in the NSD within the first 1 kHz of data are assumed to come from acoustic noise in the lab, transferred onto our laser via the spring-loaded mirror mounts in the ECDL setup. When bringing the laser on the FPI's resonance manually without scanning the FPI (figure 34), fluctuations on the order of 1 kHz are also observed on the oscilloscope and after a manual Fourier transformation, which supports the assumption made before.

A measurement of the error signal spectrum without optical feedback is done to get an idea of the linewidth of the bare DBR diode. The fast I-part of the PID servo is used to talk to the laser diode's current to hold the "free running"laser on the FP cavity for the time of the measurement. Again a minimal possible gain is used on the PID servo, to not reduce the linewidth too much by the locking scheme applied. A high resolution measurement up to 29 kHz yields $\Delta\nu_{\text{DBR, high RES}} = 2,57(1)$ MHz, whereas a high bandwidth measurement up to 200 kHz gives $\Delta\nu_{\text{DBR, high BW}} = 4,13(2)$ MHz. These results are not agreeing with each other, therefore we assume that the linewidth of the bare DBR diode must be on the order of 10 MHz, which would agree with linewidths of other commercially available DBR diodes in this wavelength range.

In section 4.3, the second experimental setup is built, where the spring-loaded movable mounts from the first setup are removed. Instead, two Risley prism pairs are used to couple the laser light into the retro-reflecting optical fiber. Now, all optical elements in the ECDL path are fixed and are bolted inside a custom-built aluminium housing. In addition, the optics in the ECDL setup are shrunk down from 1 inch optics to 1/2 inch optics to make it more compact and to reduce environmental effects such as air bursts or dust.

The PDH technique is again used to generate an error signal, which is measured with an audio analyser. Again, the PID servo is needed to hold the laser on the FPI's resonance for the time of the measurement. A high resolution measurement on the audio analyser yields a linewidth of $\Delta\nu_{2,\text{high RES}} = 5,7(2)$ kHz. This is in agreement with a high bandwidth measurement, giving a linewidth of $\Delta\nu_{2,\text{high BW, 29kHz}} = 5,576(2)$ kHz when integrated up to 29 kHz.

We have implemented a 1 m long retro-reflecting optical fiber in a long-external cavity DBR diode laser at 852 nm. We have also shown a way to eliminate standard mirror mounts in such a setup by using two Risley prism pairs to steer the beam into the optical fiber. This technique of using two prism pairs to steer the beam is not harder to align than a standard beam-walking technique with mirror mounts. With the Risley prism pairs, the beam is steered in polar coordinates, where standard mirror mounts would steer the beam in x- and y-direction. The laser system could achieve a linewidth of 72(3) kHz with approximately 435 μW of optical feedback power from a retro-reflecting

optical fiber, using standard moveable mirror mounts. By making these components fixed and using two Risley prism pairs to steer the beam, a linewidth of 5,7(2) kHz was measured. Compared to the bare DBR diode, this is a reduction in linewidth by four orders of magnitude.

Literatur

[1] 12.5mm prism wedge 2 deg vis-nir. https://www.edmundoptics.de/p/2deg-nom-125mm-dia-vis-nir-wedge-prism/33357/. accessed on May 26th 2020.

[2] Audio analyzer sr1 - dual-domain audio analyzer. https://www.thinksrs.com/downloads/pdfs/catalog/SR1c.pdf. accessed on February 16th 2021.

[3] C220tmd-b - f = 11.00 mm, na = 0.25, mounted aspheric lens, arc: 600 - 1050 nm. https://www.thorlabs.com/thorproduct.cfm?partnumber=C220TMD-B. accessed on May 26th 2020.

[4] Compact photodiode power head with silicon detector s120c. https://www.thorlabs.com/drawings/a931c1424e94ab8d-A784EC5E-CCFE-2F1D-76F9D4ED1851C291/S120C-SpecSheet.pdf. accessed on January 22nd 2020.

[5] Fundamentals of lasers. https://www.edmundoptics.com/knowledge-center/application-notes/lasers/fundamentals-of-lasers/. accessed on June 2nd 2020.

[6] Ldh3-p1/m - 30 mm cage plate collimation mount for to-3 laser diodes and m9 x 0.5-threaded aspheric lenses, metric post tap. https://www.thorlabs.com/thorproduct.cfm?partnumber=LDH3-P1/M. accessed on May 14th2020.

[7] The nist reference on constants, units and uncertainties - boltzmann constant. https://physics.nist.gov/cgi-bin/cuu/Value?k. accessed on May 19th 2020.

[8] The nist reference on constants, units and uncertainties - planck constant. https://physics.nist.gov/cgi-bin/cuu/Value?h|search_for=planck+constant. accessed on May 18th 2020.

[9] P3-780pm-fc-2 - pm patch cable, panda, 780 nm, fc/apc, 2 m. https://www.thorlabs.com/thorproduct.cfm?partnumber=P3-780PM-FC-2. accessed on May 26th 2020.

[10] P5-780pmr-p01-1 - polarization-maintaining retroreflector, 770 - 1100 nm, fc/apc connector. https://www.thorlabs.com/thorproduct.cfm?partnumber=P5-780PMR-P01-1. accessed on May 26th 2020.

[11] Prm05/m - high-precision rotation mount for Ø1/2”(12.5 mm) optics, metric. https://www.thorlabs.com/thorproduct.cfm?partnumber=PRM05/M. accessed on May 26th 2020.

[12] Thorlabs application note - risley prism scanner. https://www.thorlabs.com/images/tabimages/Risley_Prism_Scanner_App_Note.pdf. accessed on February 2nd 2021.

[13] Thorlabs laser diode controller ldc200c series operation manual. https://www.thorlabs.com/drawings/a931c1424e94ab8d-A784EC5E-CCFE-2F1D-76F9D4ED1851C291/LDC202C-Manual.pdf. accessed on January 22nd 2020.

[14] Wavelength tuning of distributed bragg reflector lasers. http://www.photodigm.com/literature/applications-notes/wavelength-tuning-in-dbr-lasers. accessed on February 15th 2021.

[15] G. Kirchhoff und R. Bunsen. Chemische analyse durch spectralbeobachtungen. *Ann. Phys. und Chemie 110, 161-189*, 1860.

[16] L. Essen and J. V. L. Parry. An atomic standard of frequency and time interval. *Nature No. 4476, 280-282*, 1955.

[17] A. L. Schawlow and C. H. Townes. Infrared and optical masers. *Phys. Rev.*, 112:1940–1949, Dec 1958.

[18] M. G. A. Bernard and D. Duraffourg. Laser conditions in semiconductors. *Phys. Status Solidi*, **1**:pp. 699, 1961.

[19] O. N. Krokhin N. G. Basov and Yu. M Popov. Production of negative temperature states in p-n junctions of degenerate semiconductors. *JETP*, **40**:pp. 1320, 1961.

[20] N. Holonyak Jr. and S. F. Bevacqua. Coherent (visible) light emission from ga ($as_{1-x}p_x$) junctions. *Appl. Phys. Lett.*, **1** (4):82–83, 1962.

[21] G. Burns F. H. Dill Jr. M. I. Nathan, W. P. Dumke and G. J. Lasher. Stimulated emissio of radiation from gaas p-n junctions. *Appl. Phys. Lett.*, **1** (3):62–64, 1962.

[22] J. D. Kingsley T. J. Soltys R. N. Hall, G. E. Fenner and R. O. Carlson. Coherent light emission from gaas junctions. *Phys. Rev. Lett.*, **9** (9):366–368, 1962.

[23] J. Crowe and R. M. Craig Jr. Gaas laser linewidth measurements by heterodyne detection. *Appl. Phys. Lett.*, **5**:72–74, 1964.

[24] Melvin Lax. Quantum Noise V: Phase Noise in a Homogeneously Broadened Maser. In P. L. Kelley, B. Lax, and P. E. Tannenwald, editors, *Physics of Quantum Electronics*, page 735, January 1966.

[25] M. Lax. Classical noise v: Noise in self-sustained oscillators. *Phys. Rev.*, **160** (2):290–307, 1967.

[26] Comptes rendus de la 13^{e} cgpm (1967). *p. 103*, 1969.

[27] P. W. Foy I. Hayashi, M. B. Panish and S. Sumski. Junction lasers which operate continuously at room temperature. *Appl. Phys. Lett.*, **17** (3):109–111, 1970.

[28] E. L. Portnoi Zh. I. Alferov, V. M. Andreev and M. K. Trukan. Alas-gaas heterojunction injection lasers with a low room-temperature threshold. *Fiz. Tekh. Polupovodn*, **75** (1):54–58, 1970.

[29] C. Wieman and T. W. Hänsch. Doppler-free laser polarization spectroscopy. *Phys. Rev. Lett.*, 36:1170–1173, May 1976.

[30] D. S. Elliott, Rajarshi Roy, and S. J. Smith. Extracavity laser band-shape and bandwidth modification. *Phys. Rev. A*, 26:12–18, Jul 1982.

[31] D. Welford and A. Mooradian. Output power and temperature dependence of the linewidth of single-frequency cw (gaal)as diode lasers. *Appl. Phys. Lett.*, **40** (10):865–867, 1982.

[32] Larry A. Coldren and T. L. Koch. Analysis and design of coupled-cavity lasers—part i: Threshold gain analysis and design guidelines. *IEEE Journal of Quantum Electronics*, 20(6):659–670, June 1984.

[33] W. T. Tsang, N. A. Olsson, R. A. Logan, R. A. Linke, B. L. Kasper, and I. P. Kaminow. Cleaved-coupled-cavity (c3) semiconductor lasers. In *International Quantum Electronics Conference*, page MII1. Optical Society of America, 1984.

[34] C. Henry. Phase noise in semiconductor lasers. *Journal of Lightwave Technology*, 4(3):298–311, 1986.

[35] B. Dahmani, L. Hollberg, and R. Drullinger. Frequency stabilization of semiconductor lasers by resonant optical feedback. *Opt. Lett.*, 12(11):876–878, Nov 1987.

[36] R. F. Kazarinov H. J. Lee B. H. Johnson N. A Olsson, C. H. Henry and K. J. Orlowsky. Narrow linewidth 1.5 μm semiconductor laser with a resonant optical reflector. *Appl. Phys. Lett.*, **51** (15):1141–1142, 1987.

[37] M. Osinski and J. Buus. Linewidth broadening factor in semiconductor lasers - an overview. *IEEE J. Quantum Electron.*, **23** (1):9–29, 1987.

[38] D. R. Hjelme, A. R. Mickelson, and R. G. Beausoleil. Semiconductor laser stabilization by external optical feedback. *IEEE Journal of Quantum Electronics*, 27(3):352–372, 1991.

[39] A. Steinbach K. B. MacAdam and C. Wieman. A narrow-band tunable diode laser system with grating feedback, and a saturated absorption spectrometer for cs and rb. *American Journal of Physics 60, 1098*, 1992.

[40] J. S. Wilson A. Arnold and M. G. Boshier. A simple extended-cavity diode laser. *Rev. Sci. Instrum.*, **69** (3):1236–1239, 1998.

[41] Kristan L. Corwin, Zheng-Tian Lu, Carter F. Hand, Ryan J. Epstein, and Carl E. Wieman. Frequency-stabilized diode laser with the zeeman shift in an atomic vapor. *Appl. Opt.*, 37(15):3295–3298, May 1998.

[42] B. Klappauf. Experimental studies of quantum chaos with trapped cesium. 1998.

[43] W. Sibbett G. P. T. Lancaster and K. Dholakia. An extended-cavity diode laser with a circular output beam. *Rev. Sci. Instrum.*, **71** (10):3646–3647, 2000.

[44] Eric D. Black. An introduction to Pound-Drever-Hall laser frequency stabilization. *Am. J. Phys. **69**(1)*, 2001.

[45] C. J. Hawthorn L. D. Turner, K. P. Weber and R. E Scholten. Frequency noise characterization of narrow linewidth diode lasers. *Opt. Commun.*, **201**:391–397, 2002.

[46] C P Pearman, C S Adams, S G Cox, P F Griffin, D A Smith, and I G Hughes. Polarization spectroscopy of a closed atomic transition: applications to laser frequency locking. *Journal of Physics B: Atomic, Molecular and Optical Physics*, 35(24):5141–5151, dec 2002.

[47] Purves G.T. Adams C.S. et al. Jundt, G. Non-linear sagnac interferometry for pump-probe dispersion spectroscopy. *Eur. Phys. J. D 27, 273–276*, 2003.

[48] Alfred Millett-Sikking, Ifan G Hughes, Patrick Tierney, and Simon L Cornish. DAVLL lineshapes in atomic rubidium. *Journal of Physics B: Atomic, Molecular and Optical Physics*, 40(1):187–198, dec 2006.

[49] D J McCarron, S A King, and S L Cornish. Modulation transfer spectroscopy in atomic rubidium. *Measurement Science and Technology*, 19(10):105601, Aug 2008.

[50] Daniel Steck. Cesium d line data. 01 2010.

[51] Qian Lin, Mackenzie A. Van Camp, Hao Zhang, Branislav Jelenković, and Vladan Vuletić. Long-external-cavity distributed bragg reflector laser with subkilohertz intrinsic linewidth. *Opt. Lett.*, 37(11):1989–1991, Jun 2012.

[52] Dali Sun, Chao Zhou, Lin Zhou, Jin Wang, and Mingsheng Zhan. Modulation transfer spectroscopy in a lithium atomic vapor cell. *Opt. Express*, 24(10):10649–10662, May 2016.

[53] S. Jackson M. Verma S. Potnis, G. J. A. Edge and A. C. Vutha. Note: A compact external-cavity diode laser, using feedback from an optical fiber. *Review of Scientific Instruments*, **88**:096102, 2017.

[54] G. P. Agrawal. *Fiber-Optic Communication Systems.* Academic Press, Boston, 1992.

[55] Wolfgang Demtröder. *Experimentalphysik 2: Elektrizität und Optik; 6th ed.* Springer, Berlin, 2013.

[56] Roy M. Howard. *Principles of Random Signal Analysis and Low Noise Design.* Wiley-Interscience, New York, 2002.

[57] P. Stoica and R. Moses. *Spectral Analysis of Signals.* Prentice Hall, New Jersey, 2005.

[58] G. H. B. Thompson. *Physics of Semiconductor Laser Devices.* Wiley, New York, 1980.

[59] Gary C. Bjorklund. Frequency-modulation spectroscopy: a new method for measuring weak absorptions and dispersions. *Opt. Lett.*, 5(1):15–17, Jan ts , url = http://ol.osa.org/abstract.cfm?URI=ol-5-1-15, doi = 10.1364/OL.5.000015.

[60] Jon H. Shirley. Modulation transfer processes in optical heterodyne saturation spectroscopy. *Opt. Lett.*, 7(11):537–539, Nov ts , url = http://ol.osa.org/abstract.cfm?URI=ol-7-11-537, doi = 10.1364/OL.7.000537.

[61] Cunyun Ye. *Tunable External Cavity Diode Lasers.* World Scientific, 2004.